Supporting Information

Colloidal Bismuth Chalcohalide Nanocrystals

D. Quarta, S. Toso, R. Giannuzzi, R. Caliandro*, A. Moliterni, G. Saleh, A.-L. Capodilupo, D. Debellis, M. Prato, C. Nobile, V. Maiorano, I. Infante, G. Gigli, C. Giannini, L. Manna, C. Giansante*

Experimental Section.

Materials. All chemicals were of the highest purity available unless otherwise noted and were used as received. Bismuth(III) acetate (Bi(Ac)$_3$; 99.99 %) was purchased from Alfa Aesar. Oleic acid (OlCOOH, technical grade, 90 %), 1-octadecene (technical grade, 90 %), bis(trimethylsylil)sulfide ((Me$_3$Si)$_2$S; synthesis grade), 1,1-dimethyl-2-selenourea (97 %), methylammonium bromide (MeNH$_3^+$Br$^-$; 98 %), tetrabutylammonium iodide (Bu$_4$N$^+$I$^-$; 98 %), iodine (99.8 %), sodium chloride (NaCl, 99.0 %), sodium iodide (NaI, 99.0 %), and lithium perchlorate were purchased from Sigma-Aldrich. Dodecyldimethylammonium bromide (Me$_2$Do$_2$N$^+$Br$^-$; ≥ 98 %), 1,1,3,3-tetramethylthiourea (98 %), trimethylsilyl bromide ((Me$_3$Si)Br; 97 %), iodotrimethylsilane ((Me$_3$Si)I; 97 %) were purchased from Alfa Aesar. Benzoyl bromide (BzBr; 97 %) was purchased from Acros Organics. Benzoyl chloride (BzCl; ≥ 98 %) was purchased from TCI Europe. 1-dodecanethiol (DoSH; ≥ 97.0 %) was purchased from Fluka.

All solvents were anhydrous and were used as received. Dichloroethylene was purchased from Merck; dimethylformamide and toluene were purchased from Sigma-Aldrich.

Syntheses. All the colloidal NCs were synthesized in three-neck flasks connected to a standard Schlenk line under oxygen- and moisture-free conditions.

In a typical synthesis yielding BiSBr NCs, 0.3 mmol (120 mg) of Bi(Ac)$_3$ and 3 mmol (850 mg) of oleic acid were mixed in 3 g of 1-octadecene. The mixture was vigorously stirred and deaerated through repeated cycles of vacuum application and purging with nitrogen at about 80 °C. The mixture was then heated to 110 °C to dissolve Bi(Ac)$_3$ until the solution became colorless and optically transparent, suggesting the complete formation of the bismuth(III)-oleate complex(es). The solution was cooled at 80 °C and repeatedly subjected to vacuum in the attempt to remove acetic acid eventually released upon the bismuth(III)-oleate complex(es) formation. The solution was then heated again under nitrogen flow while the temperature stabilized at 180°C. At this point, half equivalent of (Me$_3$Si)$_2$S (0.15 mmol; 32 µL) and one equivalent of BzBr (0.3 mmol; 35 µL) in 2 mL of octadecene were swiftly co-injected. The reaction was allowed to proceed for 15 minutes, then the heating mantle was removed and the resulting colloidal dispersion was forced to quickly reach room temperature by immersion of the reaction flask in an ice bath. After the synthesis, the reaction mixture was transferred to a nitrogen-filled glove box. The crude product was centrifuged without antisolvents, the supernatant was discarded, and the resulting pellet was redispersed in anhydrous toluene and stored in a nitrogen-filled glove-box for further use. Further purification by precipitation/redispersion of the NCs compromised their colloidal stability and were not suitable for the long-term storage; this issue was addressed by post-synthesis ligand exchange reactions (as described hereinafter). An effective tuning of the BiSBr NC morphology was somewhat achieved by employing alternative sulfur and bromine precursors, such as tetramethylthiourea and (Me$_3$Si)Br, respectively.

Similarly, the syntheses of BiSeBr, BiSCl, and BiSI NCs were carried out by employing other chalcogen and halogen precursors, such as 1,1-dimethyl-2-selenourea, elemental Se, BzCl, BzI, and (Me$_3$Si)I, as briefly discussed below.

BiSeBr NCs were synthesized in experimental conditions analogous to those used for BiSBr NCs, by using as Se precursors either 1,1-dimethyl-2-selenourea or elemental Se. Since both 1,1-dimethyl-2-selenourea and elemental Se are barely soluble in 1-octadecene, they were co-injected in a heterogeneous mixture with BzBr.

Colloidal BiSCl NCs were synthesized by co-injecting (Me$_3$Si)$_2$S and BzCl; we note that the lower reactivity of BzCl compared to BzBr required the use of 0.5 mmol to obtain BiSCl NCs from 0.3 mmol of Bi-carboxylates (compared to the 0.3 mmol of BzBr for the BiSBr NC synthesis).

The synthesis of BiSI NCs were performed by using either BzI or (Me$_3$Si)I as iodine precursor; BzI was obtained by reacting BzCl with an excess (1.5 equivalents) of NaI at 80 °C for five hours.[S1] The higher reactivity of BzI compared to BzBr required the use of 0.15 mmol to obtain BiSI from 0.3 mmol of Bi-carboxylates.

All the synthetic parameter used to obtain the colloidal Bi chalcohalide NCs are listed in Tables S1 and S2.

Table S1. Standard synthetic conditions chosen to prepare the colloidal Bi chalcohalide NCs.

Synthetic Product	Injection/Growth Temperature (°C)	Growth Time (min)	Bi precursor concentration (mM)	Oleic acid concentration (M)	E precursor concentration (mM)	X precursor concentration (mM)
BiSCl	180	15	63	0.63	32	110
BiSBr	180	15	63	0.63	32	63
BiSI	180	15	63	0.63	32	63
BiSeBr	180	60	63	0.63	32	63

Table S2. Range of the synthetic conditions yielding phase pure colloidal Bi chalcohalide NCs, which were used to attempt a control of their size and shape.

Synthetic Product	Injection/Growth Temperature (°C)	Growth Time (min)	Bi acetate concentration (mM)	Oleic acid concentration (M)	Bi:E molar ratio	Bi:X molar ratio
BiSCl	180	1 – 180	63	0.63	2, (TMS)$_2$S	0.3 – 1, BzCl
BiSCl	180	15	63	0.63	2, (TMS)$_2$S	0.6, TMSCl
BiSBr	150 – 210	1 – 180	21 – 630	0.1 – 12	2, (TMS)$_2$S	1, BzBr
BiSBr	180	15	63	0.63	2, (TMS)$_2$S	1, TMSBr
BiSBr	180	60	63	0.63	2, thiourea	1, BzBr
BiSBr	180	60	63	0.63	2, thiourea	1, TMSBr
BiSI	180	15	63	0.63	2, (TMS)$_2$S	2, BzI
BiSI	180	15	63	0.63	2, (TMS)$_2$S	2, TMSI
BiSeBr	180 – 250	60 – 180	63	0.63	2, selenourea	1, BzBr
BiSeBr	180 – 250	60	63	0.63	2, Se	1, BzBr

Morphological, Compositional, and Crystallographic Characterization. Transmission and Scanning Electron Microscopy (TEM and SEM, respectively) were used to obtain information on the NC morphology from dried colloidal dispersion and in solids thereof, respectively. Conventional TEM images were recorded with JEOL JEM 1011 and JEM 1400 Plus microscopes, operating at an accelerating voltage of 100 kV and 120 kV, respectively. Samples for analysis were prepared by dropping from a NC dispersion onto carbon-coated Cu grids and then allowing the solvent to evaporate in a vapor controlled environment. Longitudinal and lateral sizes were determined by the statistical analysis of TEM images of several hundreds of NCs with the ImageJ software. SEM images were acquired with a cold field-emission SEM JEOL JSM-7500 FA microscope working at an acceleration voltage of 10 KV and with a Carl Zeiss FE SEM SIGMA 300VP microscope, with GEMINI® technology and fully integrated inlens detector (Inlens) for secondary electrons (SE) and an angle selective backscattered electron (HDAsB) detector, was operated at 15 kV, with a-few-seconds integration times.

X-Ray Photoelectron Spectroscopy (XPS) was used to gather information on the chemical composition of the NCs. XPS spectra were recorded with a Kratos Axis Ultra[DLD] spectrometer, using a monochromatic Al Kα source operated at 20 mA and 15 kV. Wide scan analyses were carried out with an analysis area of 300 x 700 microns and a pass energy of 160 eV. High-resolution analyses on the energy ranges typical for Bi 4f, S 2p, Br 3d and I 3d signals were carried out with the same analysis area and a pass energy of 10 eV.

Energy-Dispersive X-Ray Spectroscopy (EDS) was also used for the compositional analysis of the NCs. Data were obtained at 25 KV using an Oxford X-Max 80 system with an 80 mm^2 Si drift detector (SDD).

X-Ray Diffraction (XRD) was used to probe the crystal structure of the NCs. Powder XRD patterns were acquired on lab-grade Panalytical Empyrean diffractometer operating in a parallel beam geometry and equipped with a 1.8 kW Cu Kα ceramic X-ray (45 kW), 1 mm wide incident and receiving slits, and a 40 mA PIXcel3D 2 x 2 area detector. Samples were prepared for the analysis by precipitating the NCs with ethylacetate, discarding the supernatant and drying the precipitate under a nitrogen flux. The resulting powder was grinded in a mortar to minimize preferential orientation effects, then the powders were deposited on a zero-diffraction silicon sample holder for the analysis.

Synchrotron light was used for the structural characterization of the colloidal NCs. The X-ray data were collected in two beamtime sessions at the 28ID-2 beamline of the National Synchrotron Light Source (NSLS-II) of the Brookhaven National Laboratory (proposal number 307441). The NC powder samples were put in a capillary of 1 mm diameter that was spun during measurements. A Perkin Elmer XRD 1621 digital imaging detector (2048 x 2048 pixels and 200 x 200 µm pixel size) was mounted orthogonal to the beam path in two positions optimized for pair distribution function (PDF) and X-ray powder diffraction (XPD) measurements. In the first session BiSBr NCs were measured with a beam energy of 66.18 keV (0.1874 Å) and the detector mounted 227 mm and 1368 mm downstream from the samples; in the second session BiSCl NCs was measured at a beam energy of 67.17 keV (0.1846 Å) and the detector mounted 215 mm and 1385 mm downstream from the sample. Nickel (first session) and Lanthanum hexaboride (LaB_6) (second session) were measured as standard materials to calibrate the wavelength and the detector geometry, including the sample-to-detector distance. Empty capillaries similar to those used for holding the NC samples were measured for background estimation. Diffraction images were azimuthally integrated and converted into intensity profiles versus 2ϑ and versus momentum transfer, $Q = 4\pi sin\vartheta/\lambda$, by using the FIT2D program.[S2] The PDF profiles were calculated up to interatomic distances, r, of 50 Å from the Q profiles by the program PDFGetX3.[S3] The parameters for PDF calculation (background subtraction scale factor, minimum and maximum values of Q, degree of data-correction polynomial) were optimized on individual PDF profiles to avoid large termination effects and to preserve the signal to noise ratio. Q_{max} values were 23.2 $Å^{-1}$ and 28.8 $Å^{-1}$ for BiSBr NCs and BiSCl NCs, respectively.

XPD profiles were used to identify the crystal phases among the known structural models by inquiring the POW_COD[S4] (built form COD)[S5] and PDF-2[S6,S7] databases *via* the qualitative phase analysis softwares QUALX2.0[S4] and Highscore.[S8] For the BiSBr NCs, the PDF-2 entry n. 00-075-1811, corresponding to the ICSD collection code n.31389, was identified (space group *Pnam*). For the BiSCl NCs, no existing structural model was identified by a preliminary screening, therefore

all the steps of the ab-initio structure solution (i.e., indexing, space group determination, crystal structure solution and optimization, crystal structure refinement) were undertaken by processing the XPD profile with the software EXPO2014.[S9] The structural models were refined against PDF and XPD data by using the programs PDFGUI[S10] and Fullprof.[S11] respectively. In both cases the crystal symmetry was applied to constrain lattice, displacement and atomic position parameters. The sequential use of direct (PDF) and reciprocal (XPD) space refinements was carried out to avoid overfitting and being entrapped in local minima of the χ^2 function used in least-squares procedures. It is worth noting that PDF and XPD profiles used in this analysis are not directly related by a Fourier transform operation, since the experimental setup was optimized for the two measurements. Within this approach, the optimized complementary information from direct and reciprocal space was used to drive a more efficient structural refinement.

PDF refinement was executed for interatomic distances above 1.5 Å, to avoid finite-size artifacts in the low r range, and up to 45 Å, with a step of 0.01 Å. As a first step, the scale factor, lattice parameters, peak shape parameters Q_{broad} (peak broadening from increased intensity noise at high Q) and $delta1$ (coefficient for $1/r$ contribution to the peak sharpening) parameters were refined separately, i.e. by keeping constant all the other parameters. As a second step, anisotropic atomic displacement parameters were included in the refinement, then the atomic position parameters were refined in a last step. More elaborated refinements were carried out by using scripts developed within the DiffPy-CMI framework,[S12] which implements procedures able to refine a model consisting of a sum of two crystal phases or to account for the shape of the NCs.

XPD refinement was carried out by the Rietveld method[S13] by considering the following: i) zero-shift; ii) background parameters; iii) scale factor and profile parameters *i.e.*, full width at half maximum and peak asymmetry; iv) crystal structure parameters, *i.e.,* lattice parameters, atomic fractional coordinates, isotropic displacement parameters, and anisotropic spherical harmonics parameters for the crystallite shape.[S14] In the last step of the refinement, all parameters are simultaneously refined.

The refinement parameters of PDF and XPD profiles are reported in Tables S3 and S4, respectively.

The program RootProf was used to convert the XPD profiles in the $CuK_{\alpha1}$ wavelength,[S15] which was done to facilitate visual comparison and to perform qualitative and semi-quantitative analysis to identify crystalline impurities from the PDF profile of the BiSCl NC sample.

Table S3. Refinement parameters derived from the PDF fits. R_w is the weighted agreement factor between observed and calculated PDF, Delta1 is the coefficient for $1/r$ contribution to the peak sharpening, Q_{broad} describes the peak broadening from increased intensity noise at high $Q,$ $SP_{diameter}$ is the particle diameter for PDF shape damping function.

	BiSBr	**BiSCl**
R_w	0.068	0.253
Delta1	1.55	1.43
Q_{broad}	0.015	0.013
$SP_{diameter}$ (Å)	74.9	71.9
a,b,c (Å)	8.179, 9.886, 4.076	7.903, 4.090, 9.146

Table S4. Figures of merit obtained by the XPD refinement. Agreement factors provided by Fullprof at the end of the Rietveld refinement. R_p is the agreement factor between observed and calculated profile, R_{wp} is the weighted- profile reliability parameter, χ^2 is the chi-squared value, GoF is the Goodness of Fit.

	BiSBr	BiSCl
R_p (%)	5.34	14.1
R_{wp} (%)	6.29	19.0
χ^2	1.27	0.76
GoF	1.1	0.87

Optical Characterization. The optical properties of the Bi chalcohalide NCs were investigated on both colloidal dispersions and thin films. A PerkinElmer UV/Vis/NIR spectrophotometer (Lambda 1050) was used to measure transmission and reflectance spectra of the NCs in the 300-1600 nm range; a 150 mm InGaAs integration sphere was used to acquire reflectance spectra. The optical band gap values of the NCs was estimated by Tauc analysis.[S16,S17]

A Dektak contact profilometer (D150 Veeco) was used to determine the thickness of the casted NC films and, therefore, to estimate the NC absorption coefficients.

Ultraviolet Photoelectron Spectroscopy (UPS) was used to determine the Fermi and valence band energies of the NC solids. UPS spectra were recorded by using the same spectrometer as per the XPS characterization. A He I (21.22 eV) discharge lamp was used as the photon source; spectra were acquired on an area of 55 µm in diameter, at a pass energy of 10 eV and with a dwell time of 100 ms. The work function and the position of the valence band maximum versus the Fermi level were estimated as described elsewhere.[S18]

Theoretical Calculations. Density Functional Theory (DFT) simulations were run to infer the electronic band structure of the Bi chalcohalide NCs. The calculations were run through the VASP code[S19] within the plane augmented wave framework.[S20] The PBE functional[S21] was adopted throughout and complemented with the Tkatchenko-Scheffler correction[S22] to accurately reproduce dispersive forces. When not otherwise specified, the following settings were adopted. The plane wave kinetic energy cutoff was set to 400 eV for band structure evaluation and to 500 eV for the remaining simulations (*e.g.* geometry optimizations). The reciprocal space was sampled through a uniform, Γ-centered grid with $0.28/2\pi$ Å^{-1} point spacing. For all the studied systems, the cell parameters and atomic positions were optimized to the closest energy minimum. Both the geometry optimization and self-consistent procedures were stopped when the energy difference between two consecutive steps was lower than 10^{-6} eV. Spin Orbit Coupling (SOC) generally neglected, as we observed its effect to be negligible on geometries and energy differences (Table S5). The effect of SOC on the band structure is discussed in the text. Surfaces and isostructures were drawn with the VESTA software.[S23]

Surface Chemistry and Thin Film Fabrication. The chemical species at the surface of as-synthesized NCs were replaced by ligand exchange reactions at room temperature either in the solution phase or in the solid phase. The oleyl-based ligands coming from the synthetic procedure were exchanged for either 1-DoSH or $Me_2Do_2N^+X^-$ in toluene and for $MeNH_3^+X^-$ in dimethylformamide. The $Me_2Do_2N^+I^-$ salt was obtained by anion exchange reactions in toluene solution of $Me_2Do_2N^+Br^-$ with a large excess of NaI. The ligand exchange reactions were carried out by adding aliquots of 100 mM solutions of the replacing ligands either in toluene or dimethylformamide up to one ligand per Bi atom; the dispersion was centrifuged, the supernatant discarded, and the resulting NC pellet redispersed in the solvent used for the replacing ligand. Thin films of the NCs for optical measurements were deposited onto glass slides by drop casting toluene dispersions of the as-synthesized NCs. Solid films of the NCs for photoelectrochemical measurements were deposited onto conductive (Indium Tin Oxide coated-) glass slides by spin casting toluene dispersions of the NCs coordinated by $Me_2Do_2N^+X^-$ ligands; the as-casted NCs were further ligand exchanged with ammonium halide in dimethylformamide, then the NC solid was rinsed with dimethylformamide; the deposition cycle was repeated up to eight times, then annealed at 180 °C.

Nuclear Magnetic Resonance (NMR) and Fourier-Transform Infrared (FTIR) spectroscopies were used to characterize the chemical species at the surface of the as-synthesized and ligand-exchanged NCs. ^{1}H-NMR spectra of toluene-d8 dispersions of the Bi chalcohalide NCs were recorded with a Bruker AV400 spectrometer operating at 400 MHz at 293 K. FTIR measurements in the 7000-400 cm^{-1} spectral range were carried out on NCs deposited on silicon substrates using a Jasco FT/IR 6300 spectrophotometer apparatus operating in transmission mode at a resolution of 4 cm^{-1}.

Photoelectrochemical Characterization. The (photo)electrochemical properties of the Bi chalcohalide NCs were measured for solid films deposited on a conductive substrate serving as the working electrode with an active area of about 1 cm^2. Electrochemical measurements were carried out with an AUTOLAB PGSTAT302N potentiostat in a 0.1 M Bu$_4$N$^+$PF$_6^-$ anhydrous dichloromethane electrolyte solution. A platinum foil served as the counter electrode (area 4 cm^2) and an Ag/AgCl electrode was used as the reference. All the potentials were referred to as the Ag/AgCl reference electrode in the abovementioned electrolyte solution. For the photoelectrochemical measurements Bu$_4$N$^+$I$^-$ (0.01 M) and I$_2$ (0.001 M) were added to the electrolyte solution as redox couple. A module composed of 7 white light emitting diodes (LEDs) with focusing optics (Luxeon, LXML-PWC2) was employed for 1-sun illumination. The module was powered with a Keithley 2400 source meter and calibrated with a reference solar cell (Newport). A UV cutoff filter (λ > 420 nm) was placed in front of the LEDs. The path length of the electrolyte was $\sim$ 5 mm. The incident photon to current conversion efficiency (IPCE) was measured at a constant bias of 0.25 V vs Ag/AgCl (KCl sat) from 360 to 840 nm in steps of 40 nm. A Xenon arc lamp (Newport, 140 W, 67005) coupled with a computer-controlled monochromator (Newport Cornerstore 260 Oriel 74125) was used to obtain the action spectrum, whereas the power of the incident light was measured with a power meter (Newport, 2936-C) and a UV Silicon Detector (Oriel 71675). The electrochemical impedance spectroscopy (EIS) measurements were performed in 0.1 M LiClO$_4$ acetonitrile solution in dark conditions by scanning the potential from -0.1 to +1.0 V vs Ag/AgCl (KCl sat) with 10 mV AC potential in the frequency range from 10^{-1} to 10^5 Hz. The spectra were fitted by using the Z-view software (Scribner Associates Inc., USA).

Colloidal BiSBr NCs.
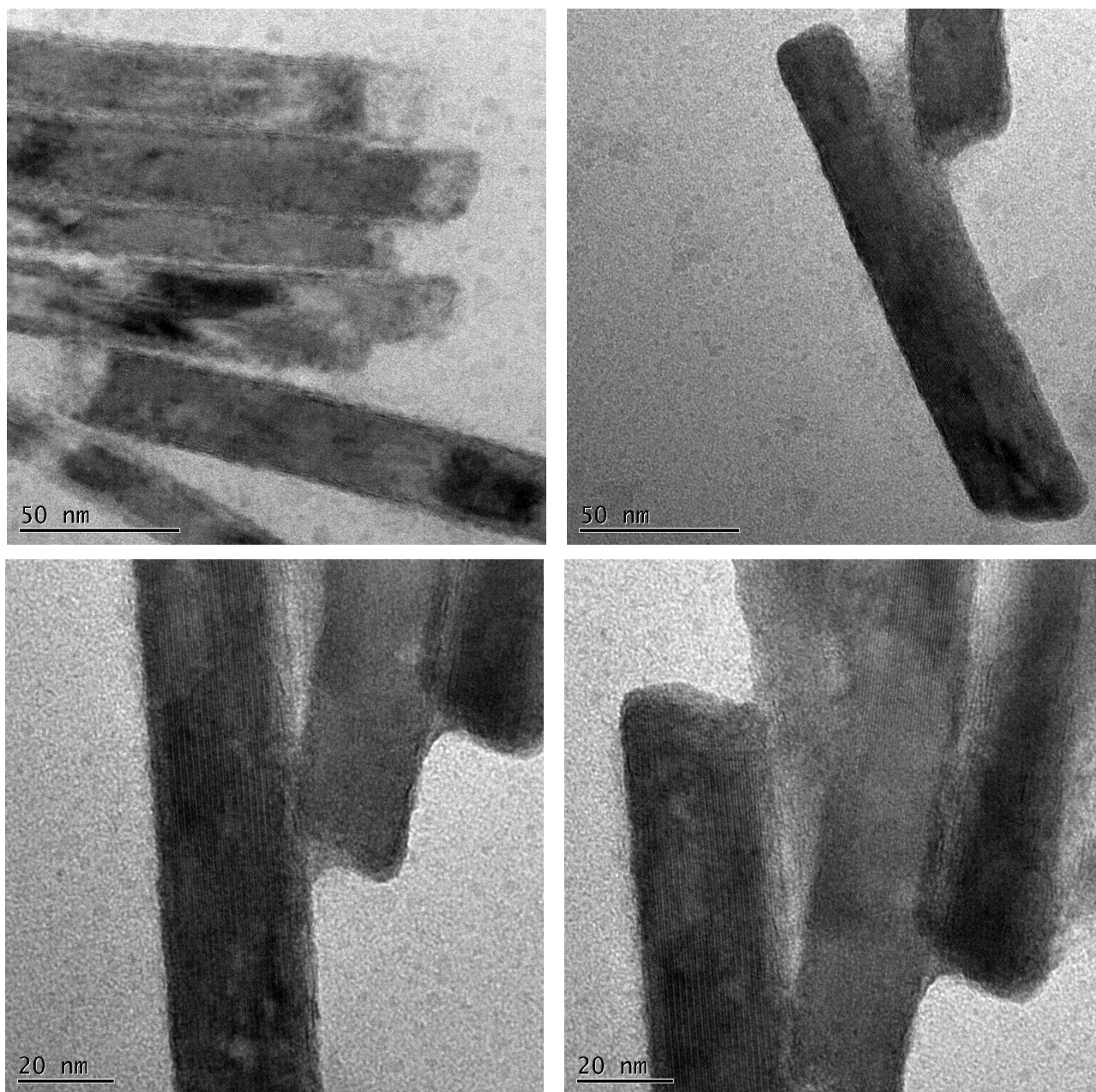
Figure S1. TEM images of the colloidal BiSBr NCs.
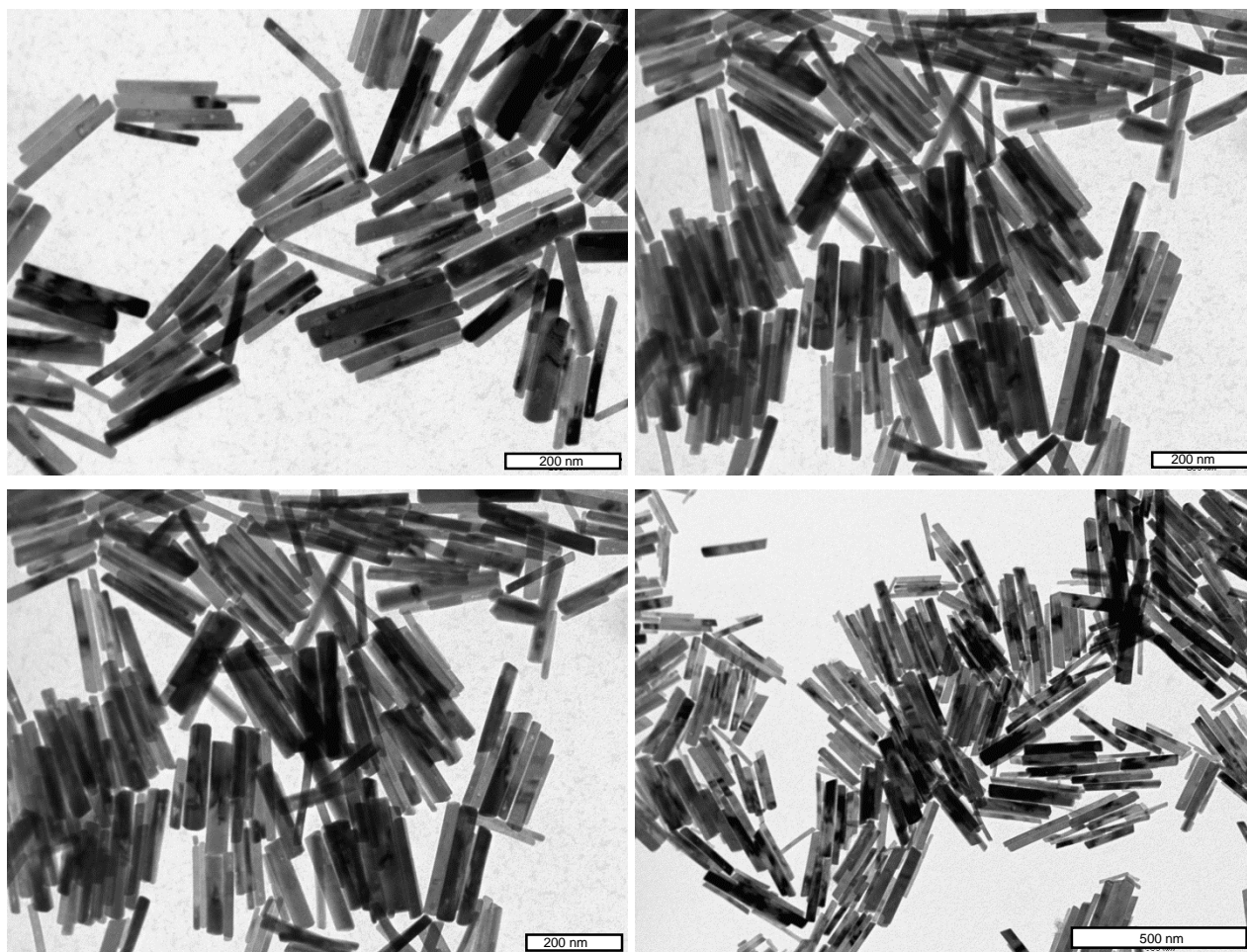
Figure S2. TEM images of the colloidal BiSBr NCs prepared by using bis(trimethylsilyl)sulfide and benzoylbromide as S and Br precursors, respectively.
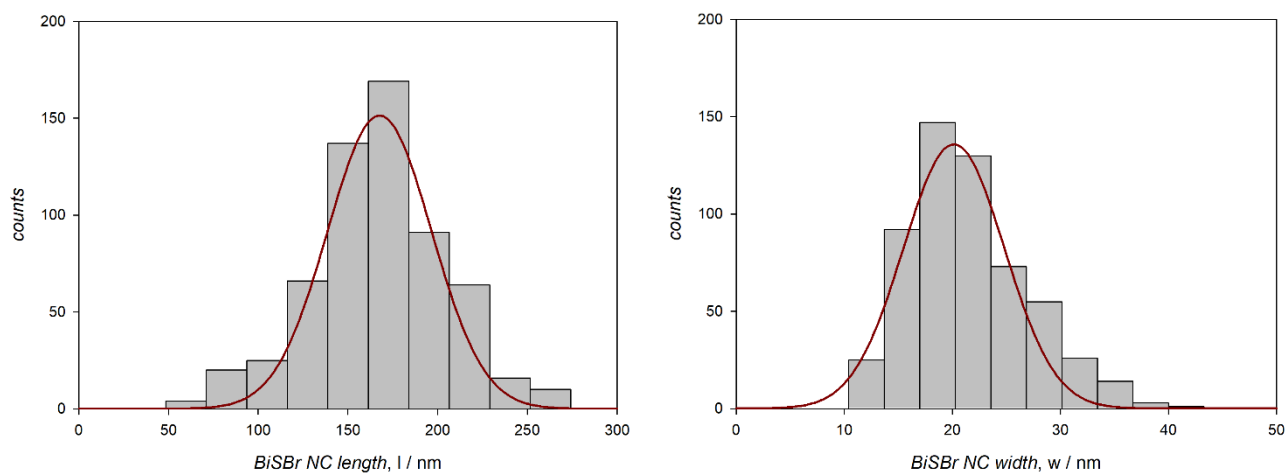
Figure S3. Polydispersity of both the length (left) and the width (right) of the colloidal BiSBr NCs.
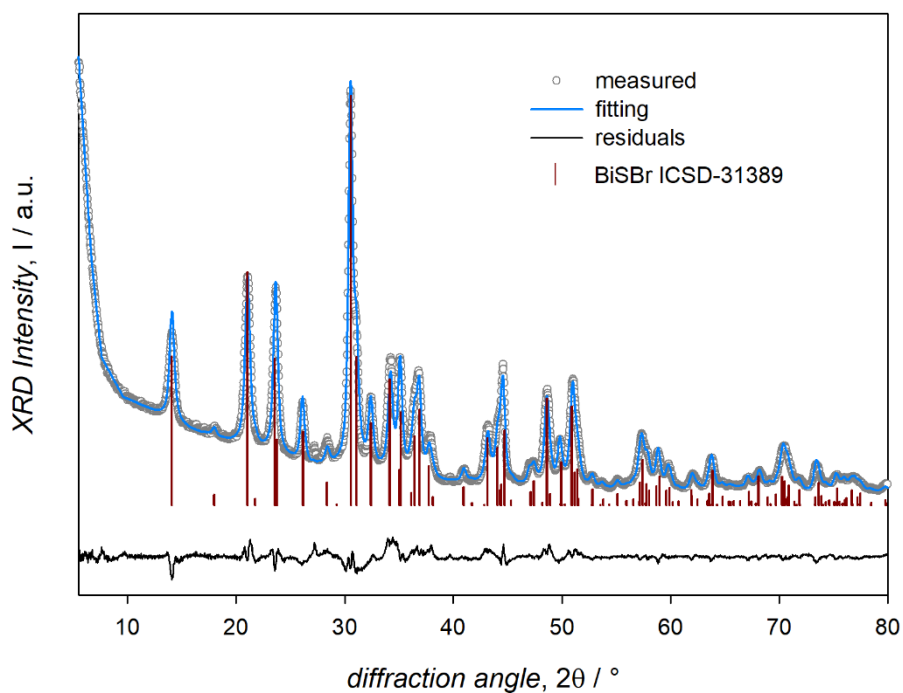
Figure S4. Rietveld refinement of the XRD pattern of the as-synthesized colloidal BiSBr NCs acquired with a lab-grade diffractometer.
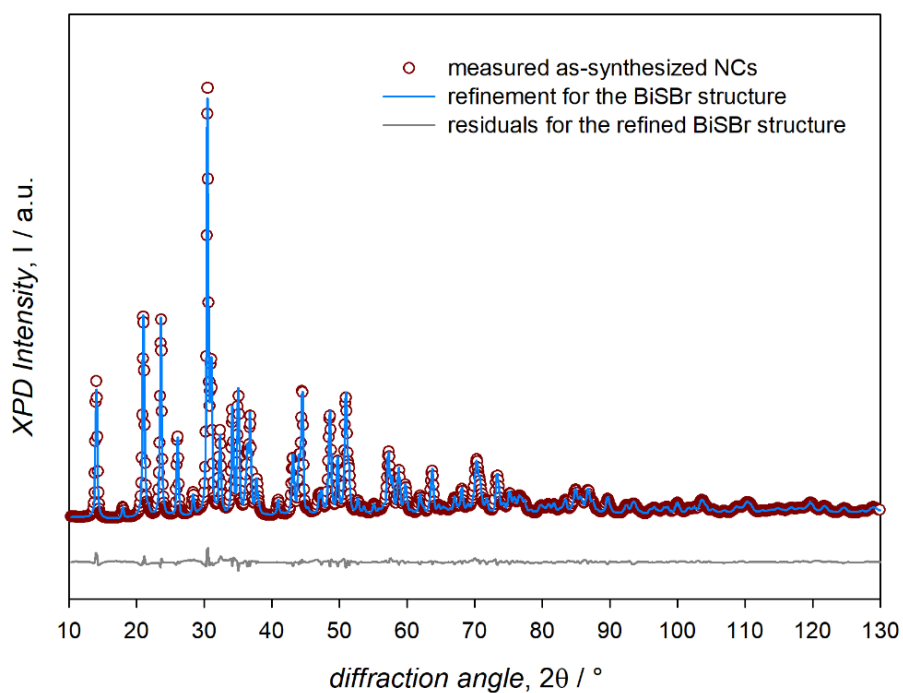
Figure S5. Expanded Figure 1b; Rietveld fitting of the synchrotron XPD diffractogram of the BiSBr NCs (to facilitate the comparison with data collected on lab-grade setups, the 2θ values of the XPD horizontal axis were converted to emulate the CuKα$_1$ radiation).
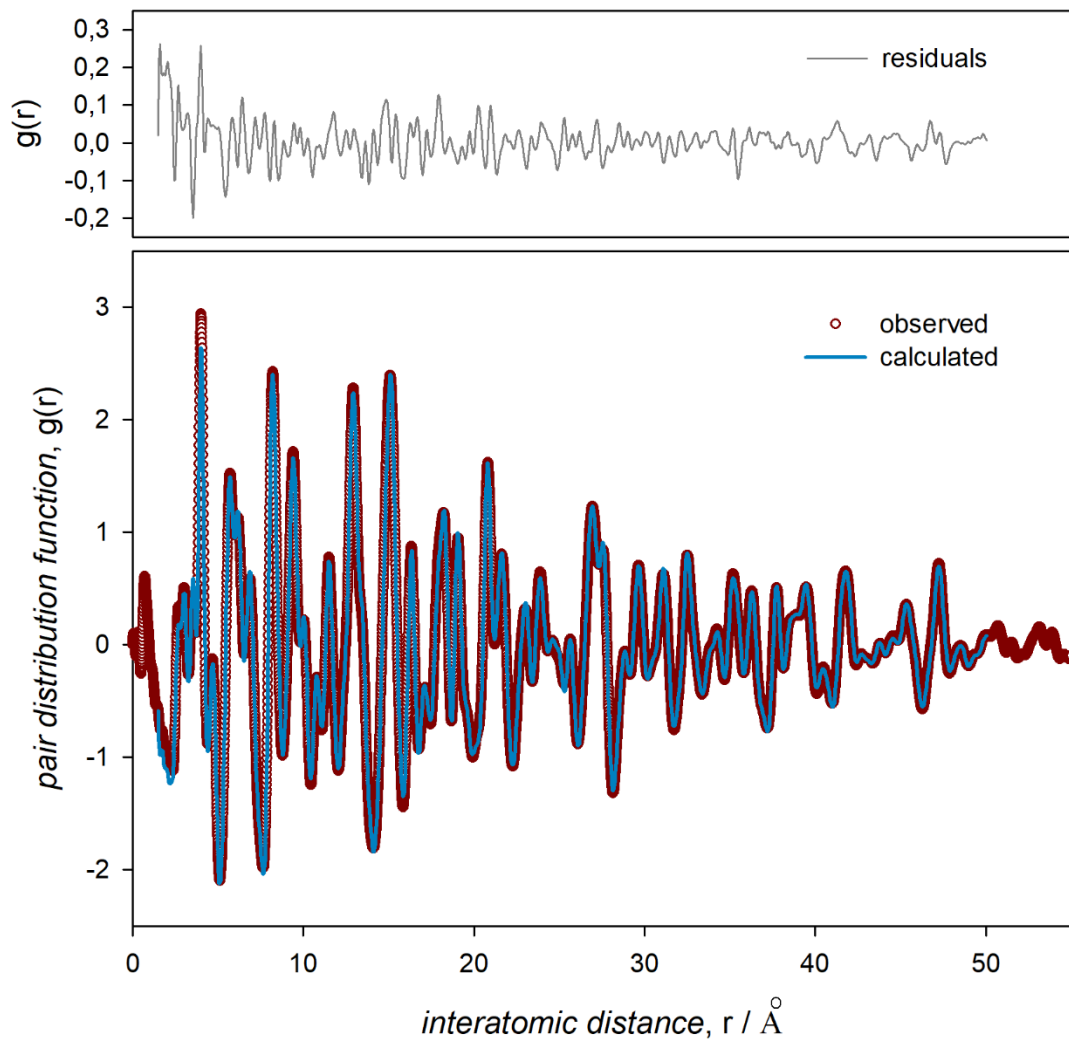
Figure S6. PDF profile of the as-synthesized colloidal BiSBr NCs.
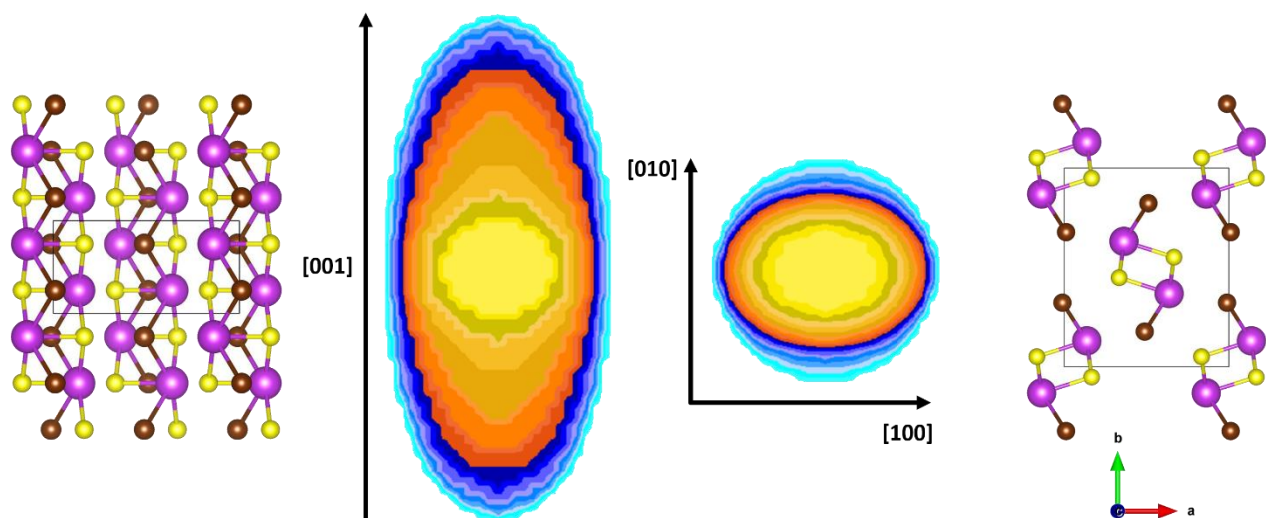
Figure S7. Image of the refined BiSBr crystallite spherical harmonics diagram.
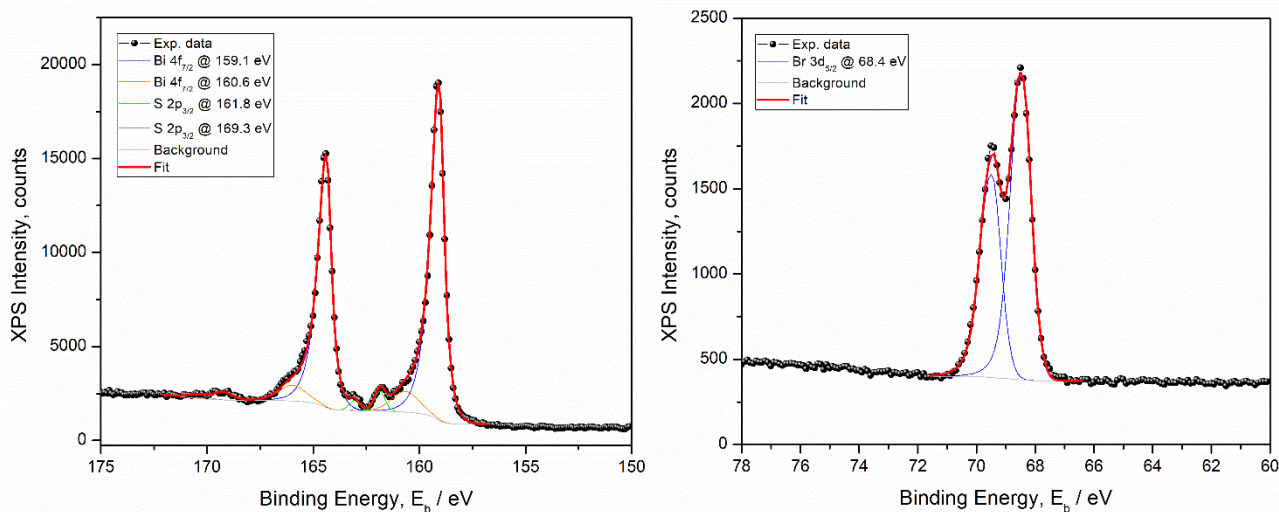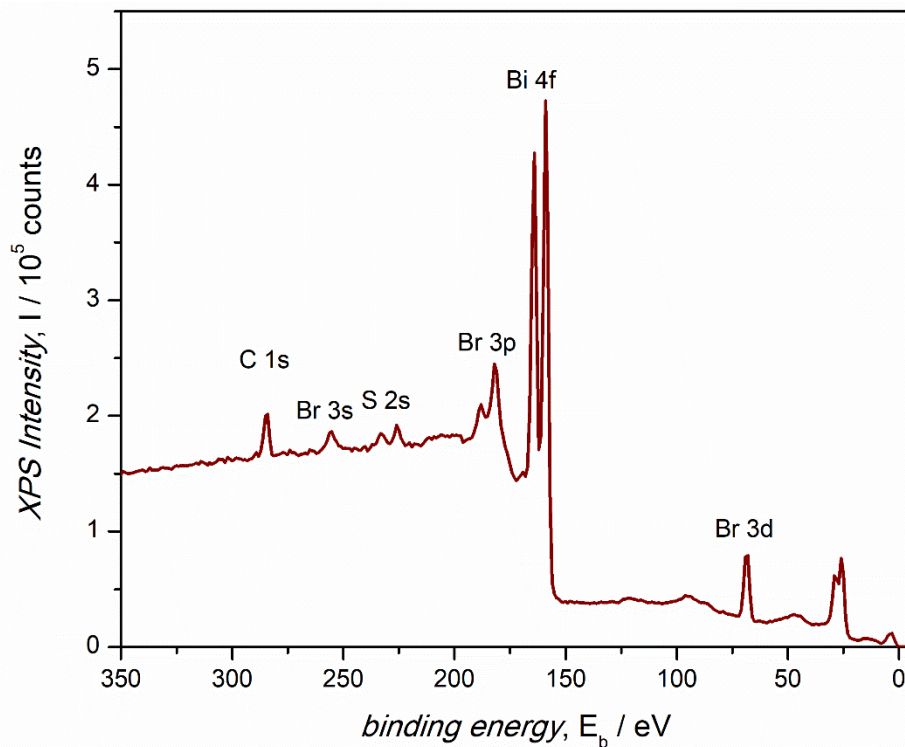
Figure S8. top) XPS spectra of the as-synthesized BiSBr NCs showing a Bi rich composition (Bi 39.0 %, S 28.9 %, Br 32.1 %). bottom) high-resolution XPS spectra showing details of the Bi 4f and S 2p region (left) and of the Br 3d region (right); the Bi 4f region shows the presence of a minor component consistent with Bi(III) species, along with a main component ascribable to BiSBr. Such a minor component could be related either to surface Bi atoms that experience different surroundings from the inner Bi atoms or to the presence of amorphous species (as-synthesized BiSBr NCs are not properly purified, as evident by NMR spectra).
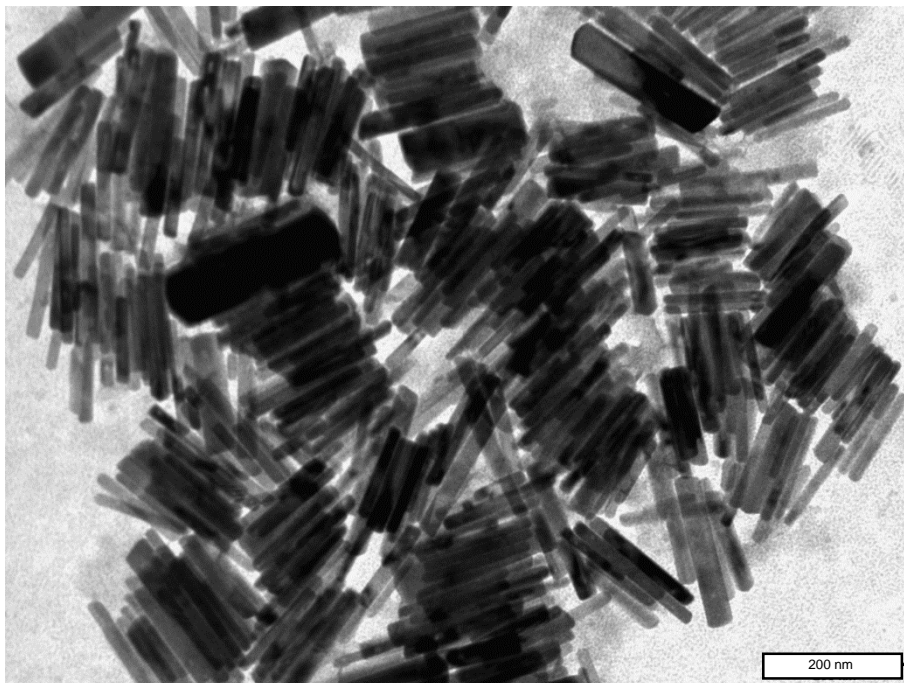
Figure S9. TEM images of the colloidal BiSBr NCs prepared with an accretion time of 150 °C. Low contrast particles could be the result of the poor purification of the as-synthesized NCs.
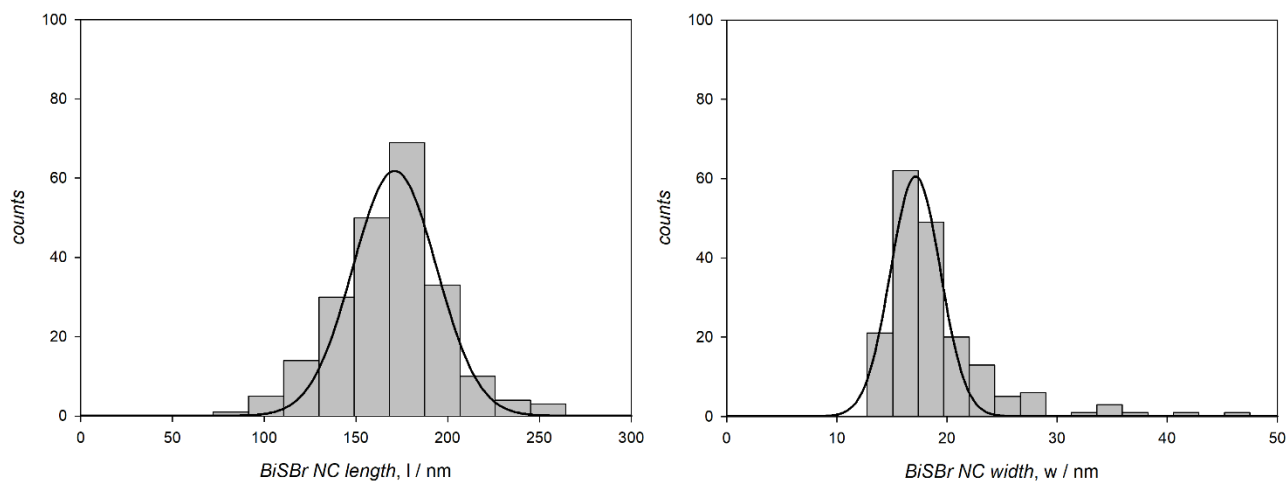
Figure S10. Polydispersity of both the length and the width of the colloidal BiSBr NCs prepared with an accretion time of 150 °C.
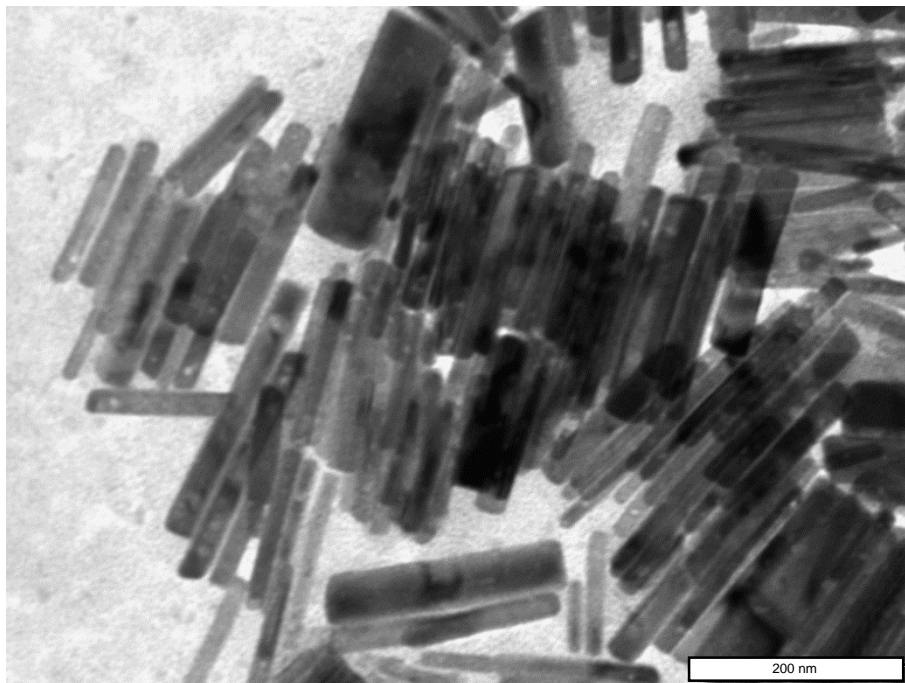
Figure S11. TEM images of the colloidal BiSBr NCs prepared with an accretion time of 210 °C. Low contrast particles could be the result of the poor purification of the as-synthesized NCs.
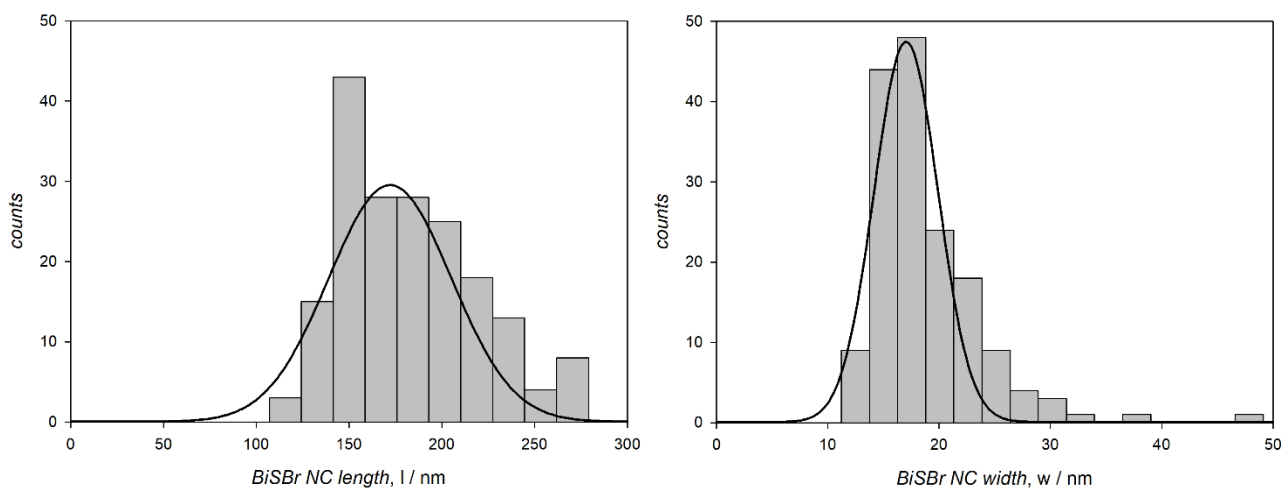
Figure S12. Polydispersity of both the length and the width of the colloidal BiSBr NCs prepared with an accretion time of 210 °C.
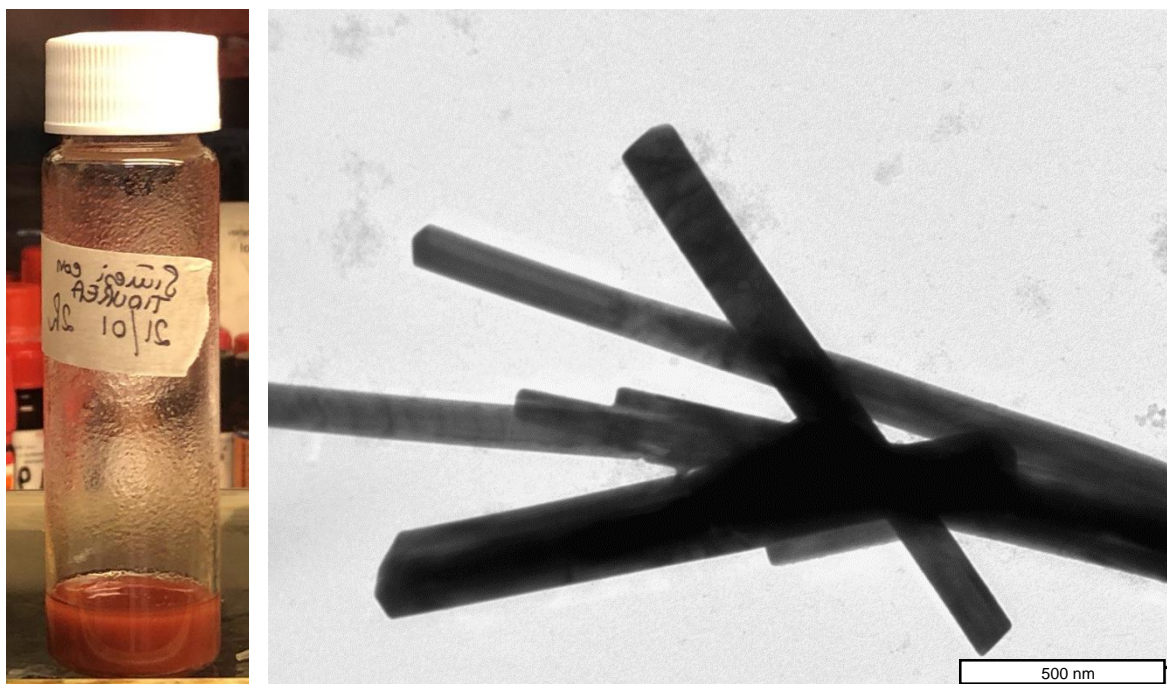
Figure S13. TEM images of the colloidal BiSBr NCs prepared by using 1,1,3,3-tetramethylthiourea and benzoylbromide as S and Br precursors, respectively. Low contrast particles could be the result of the poor purification of the as-synthesized NCs.
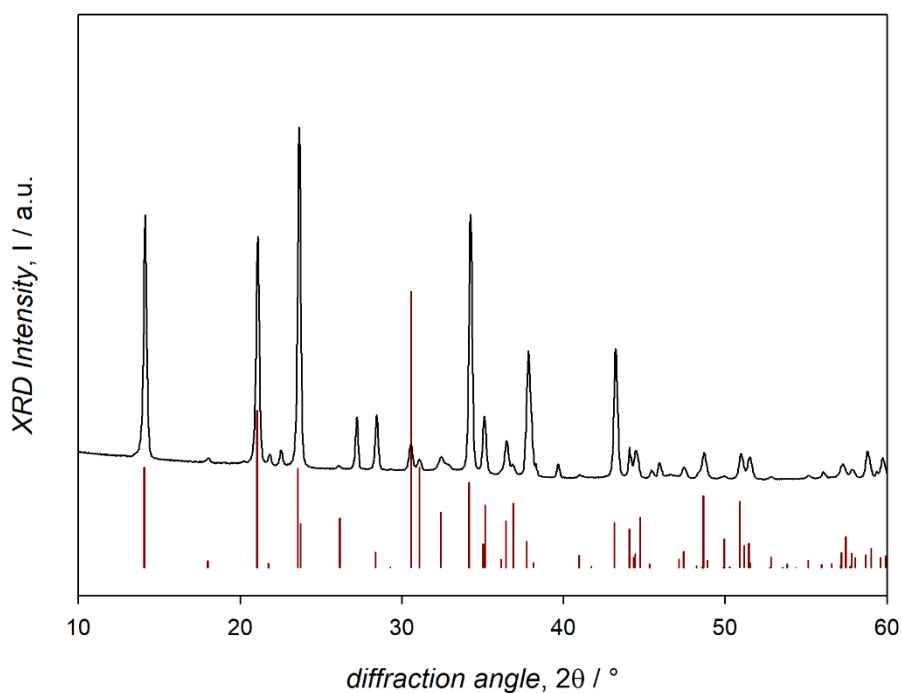
Figure S14. XRD pattern of colloidal BiSBr NCs prepared by using 1,1,3,3-tetramethylthiourea and benzoylbromide as S and Br precursors, respectively.
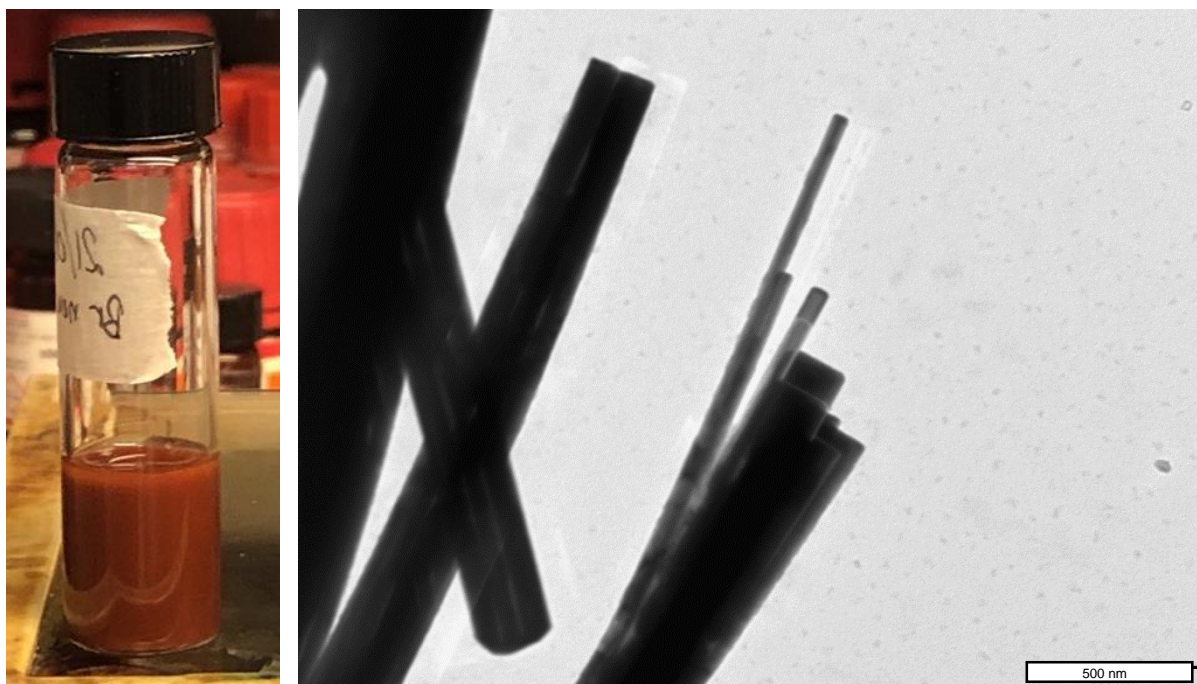
Figure S15. TEM images of the colloidal BiSBr NCs prepared by using 1,1,3,3,-tetramethylthiourea and trimethylsylilbromide as S and Br precursors, respectively. Low contrast particles could be the result of the poor purification of the as-synthesized NCs.
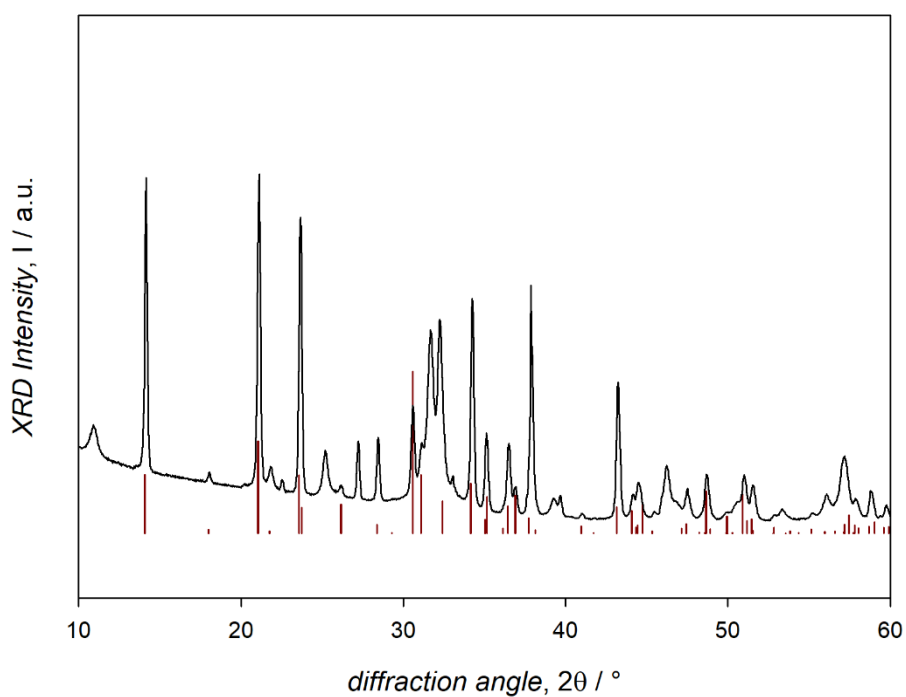
Figure S16. XRD pattern of colloidal BiSBr NCs prepared by using 1,1,3,3-tetramethylthiourea and trimethylsylilbromide as S and Br precursors, respectively.
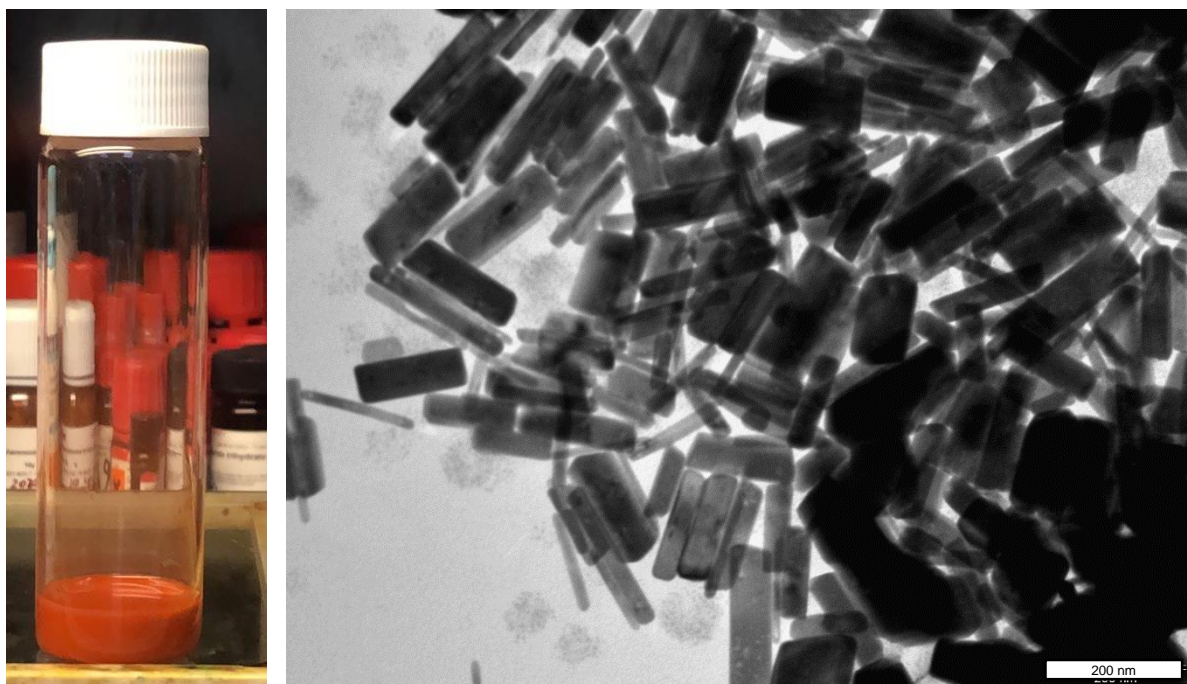
Figure S17. TEM images of the colloidal BiSBr NCs prepared by using bis(trimethylsilyl)sulfide and trimethylsylilbromide as S and Br precursors, respectively. Low contrast particles could be the result of the poor purification of the as-synthesized NCs.
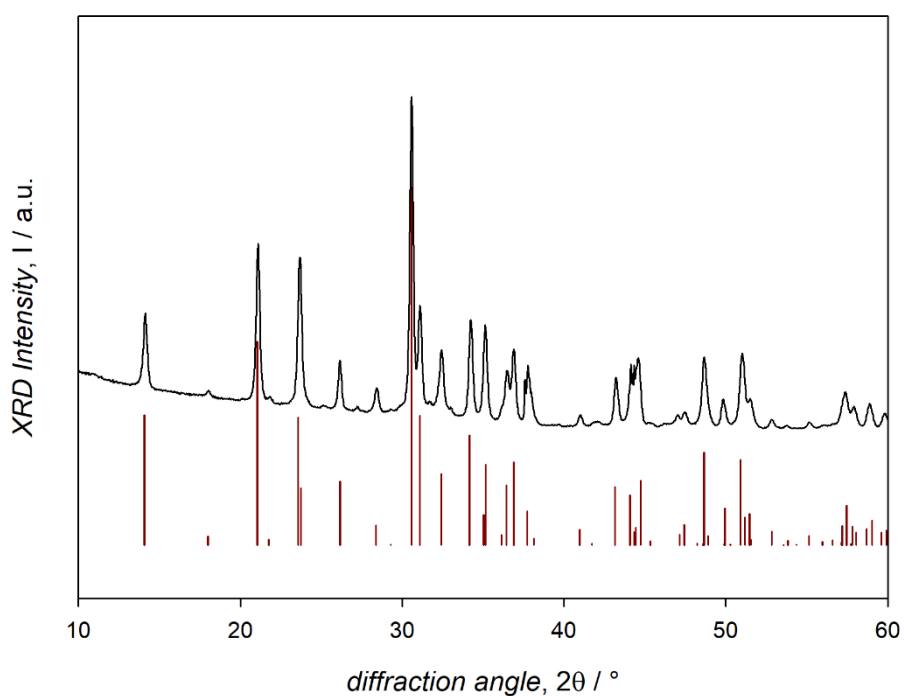
Figure S18. XRD pattern of colloidal BiSBr NCs prepared by using bis(trimethylsilyl)sulfide and trimethylsylilbromide as S and Br precursors, respectively.
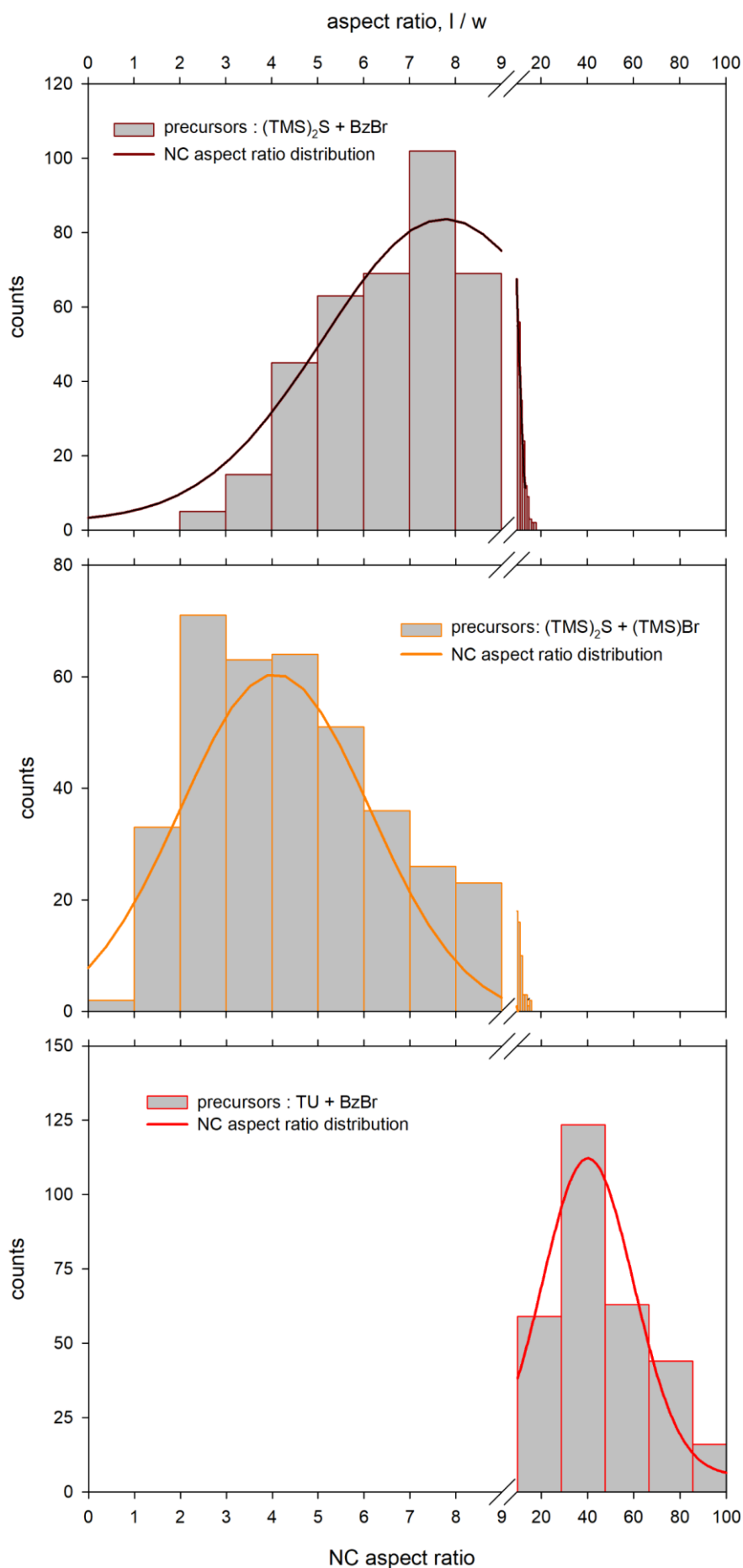
Figure S19. Polydispersity of the aspect ratio of the elongated BiSBr NCs prepared with different precursors.

Colloidal BiSeBr NCs.
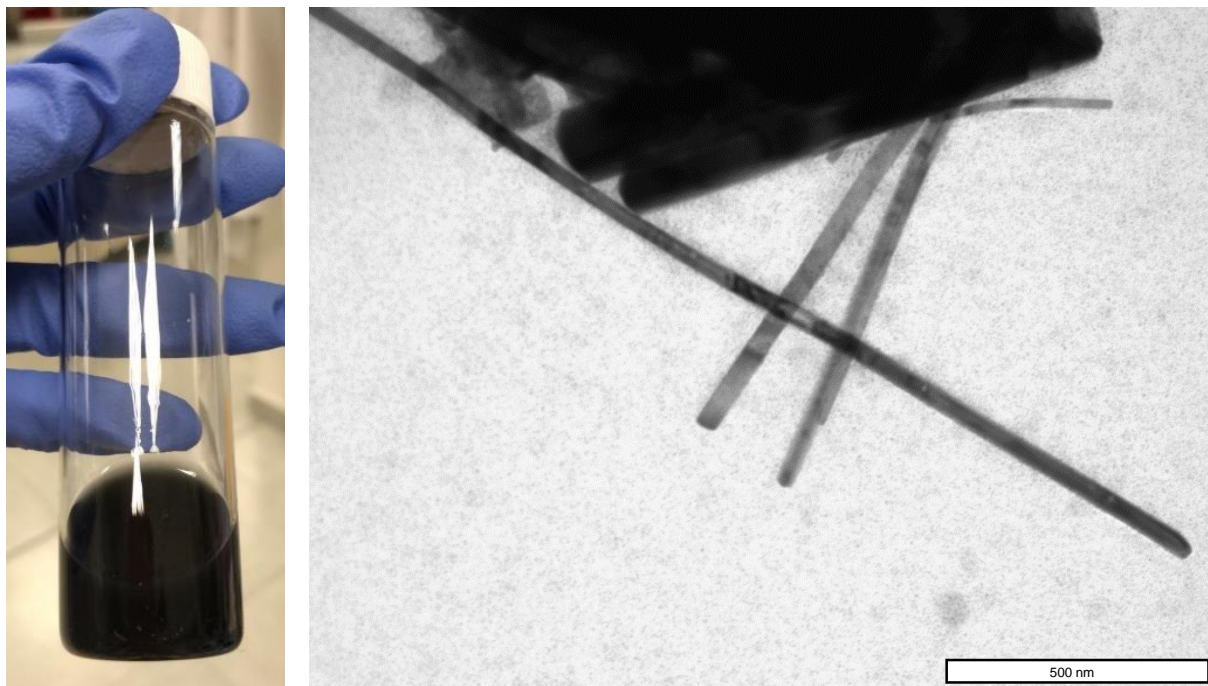
Figure S20. Daylight picture of a colloidal BiSeBr NC dispersion and TEM image of the NCs. Low contrast particles could be the result of the poor purification of the as-synthesized NCs.
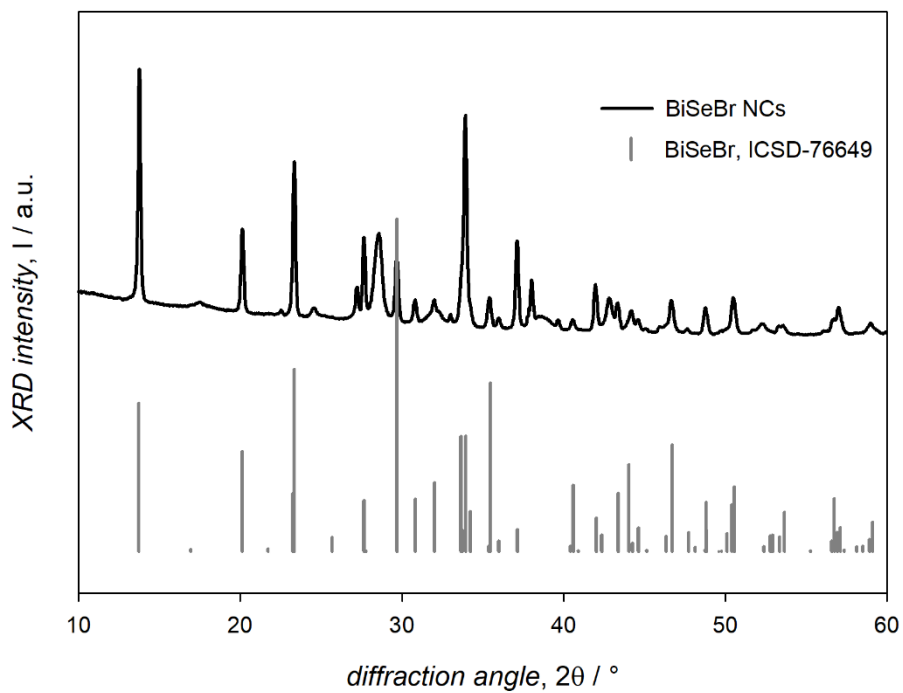
Figure S21. XRD pattern of the as-synthesized colloidal BiSeBr NCs.

Colloidal BiSI NCs.
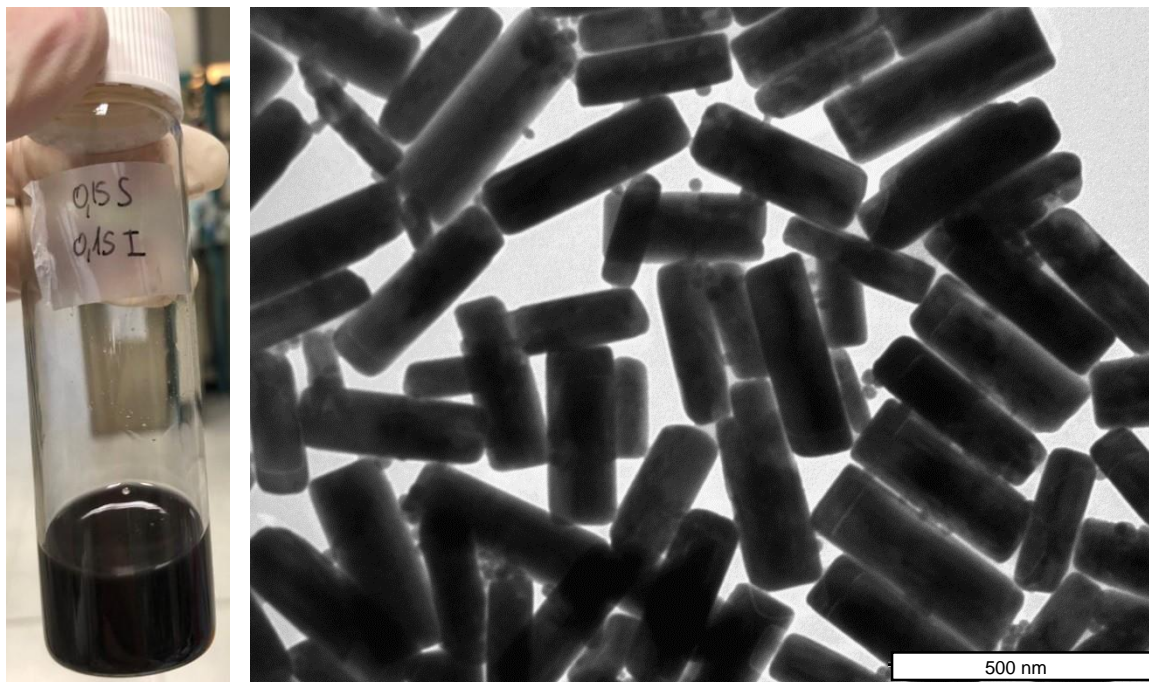
Figure S22. Daylight picture of a colloidal dispersion of BiSI NCs and a TEM image of the NCs prepared by using bis(trimethylsilyl)sulfide and benzoyliodide as S and I precursors, respectively.
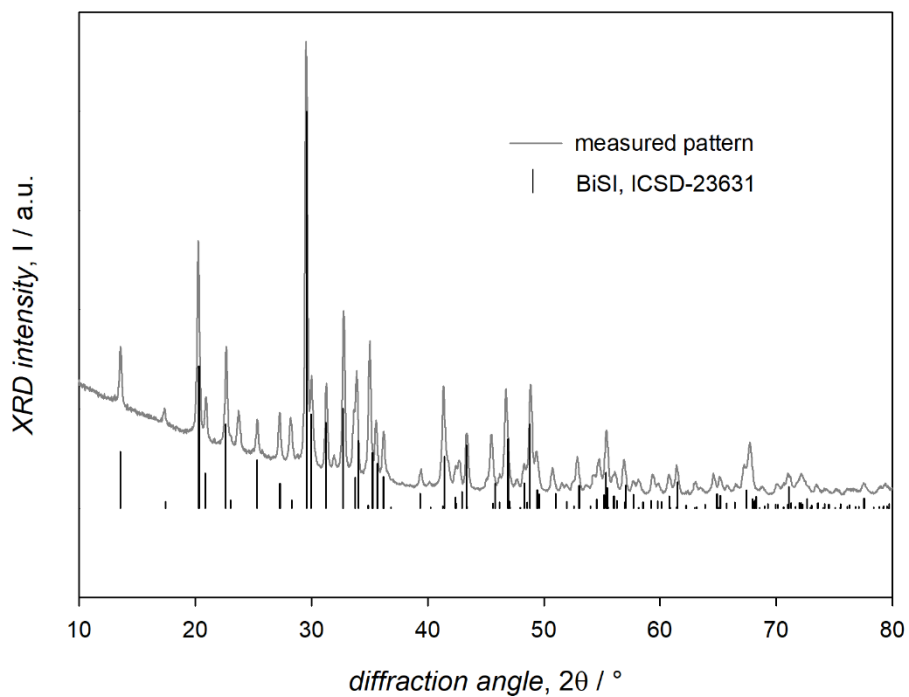
Figure S23. XRD pattern of the colloidal BiSI NCs.

Colloidal BiSCl NCs.
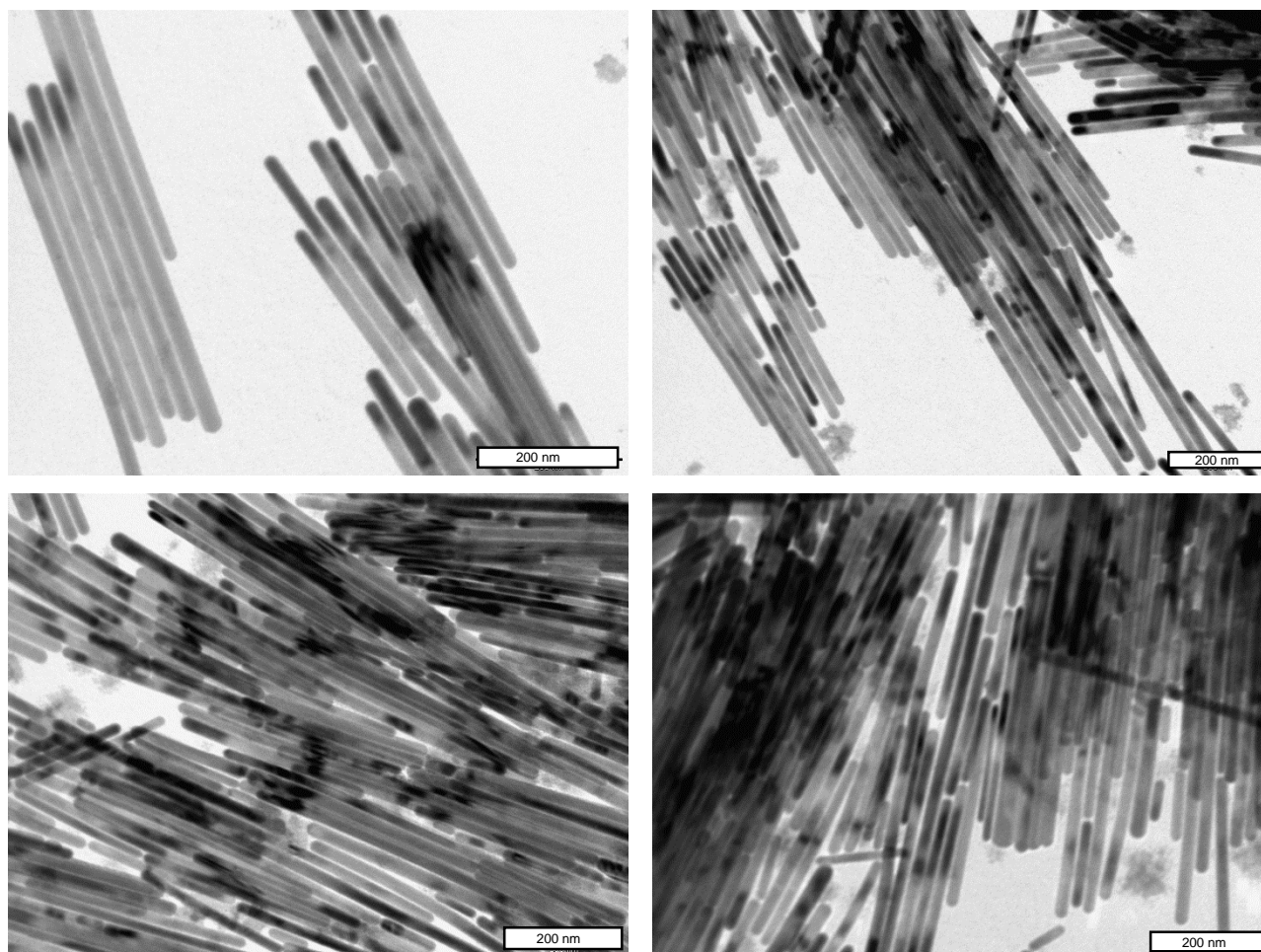
Figure S24. TEM images of the colloidal BiSCl NCs.
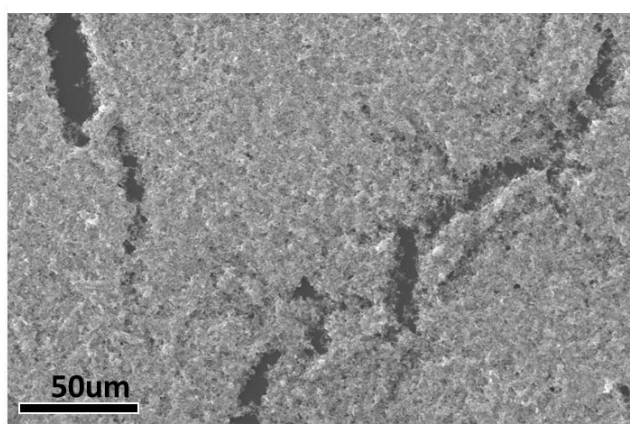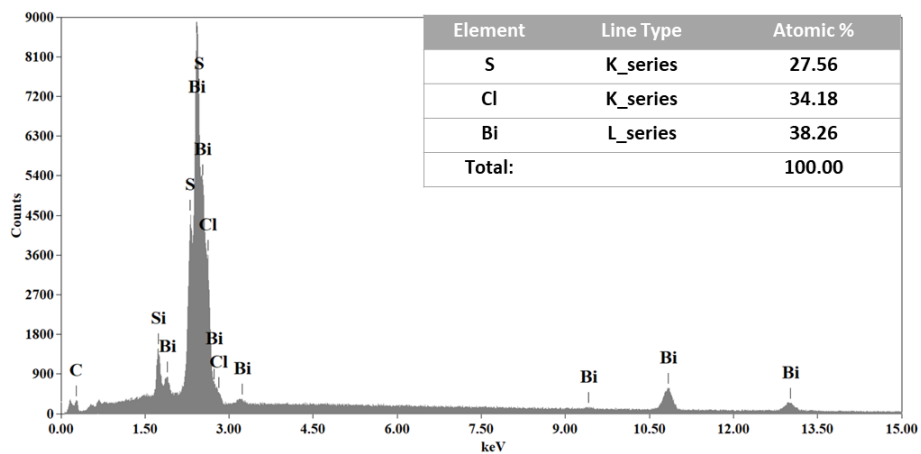
Figure S25. SEM-EDS data for the colloidal BiSCl NCs.
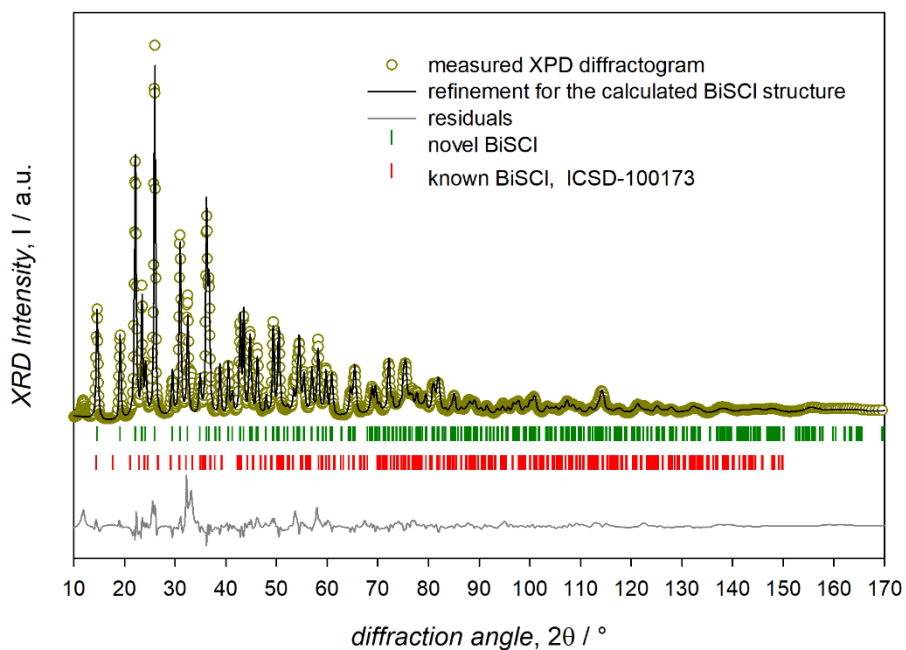
Figure S26. Expanded Figure 2a.

Ab initio structure determination of BiSCl.

The unit cell determination process was performed by the indexing program *N-TREOR09*,[S24] implemented in *EXPO2014*. 48 most intense peaks in the 2ϑ range 1.7-11.8° were located and used to determining the unit cell parameters. At the end of the indexing process, a list of six most plausible candidate cells was provided by the EXPO2014 graphic interface and the most probable one (*i.e.*, an orthorhombic cell characterized by the largest M_{20} figure of merit[S25] and unit cell parameters *a*=7.910(5), *b*=4.0994(19), *c*=9.154(4) Å) was selected to perform the space group determination step. This was carried out: i) by estimating the integrated intensities, *via* a full pattern decomposition process exploiting the selected unit cell parameters, the expected unit cell content and by assuming the largest Laue symmetry with no extinction conditions, compatible with the orthorhombic crystal system (*i.e.*, space group *Pmmm*); ii) by performing a statistical analysis of the integrated intensities, in order to detect systematic absences and calculate a probability value associated to the different possible extinction symbols compatible with the identified crystal system.[S26] At the end of the space group determination process the most plausible crystal symmetry *Pnma* (#62) was selected and used in the next steps. The integrated intensities estimates were processed by Direct Methods to carry out the structure determination process: they provided 11 different sets of phases ranked according to a combined figure of merit (CFOM). The first set of phases was automatically explored by EXPO2014, obtaining a provisional structural model that was refined and optimized by a Fourier recycling approach.[S27] The resulting structural model consisting of five atoms was carefully analyzed and modified by graphic tools: two false sulphur atoms were deleted and one chlorine atom was relabeled sulphur. The three-atoms crystal structure so obtained was preliminary refined by Rietveld method, then further optimized by the Fullprof package (see Table S4).
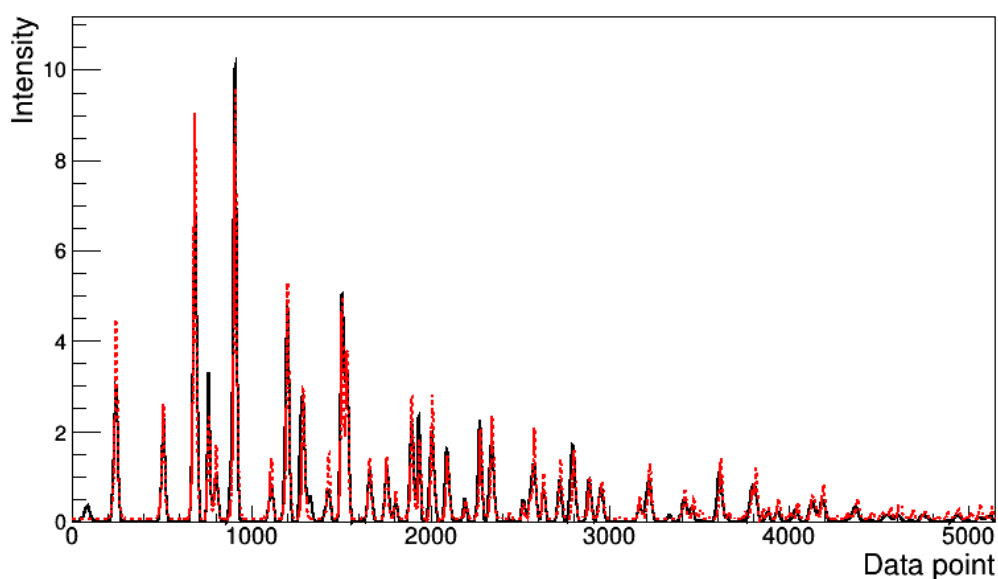

Figure S27. Result of the semi-quantitative analysis performed by the MultiFit approach implemented into RootProf program. The observed XPD profile (black line) has been background-subtracted, rescaled and fitted with the XPD profile calculated from the refined model of BiSCl (red line). The weight fraction of the crystal phase has been estimated from the fitted value of its multiplicative constant.
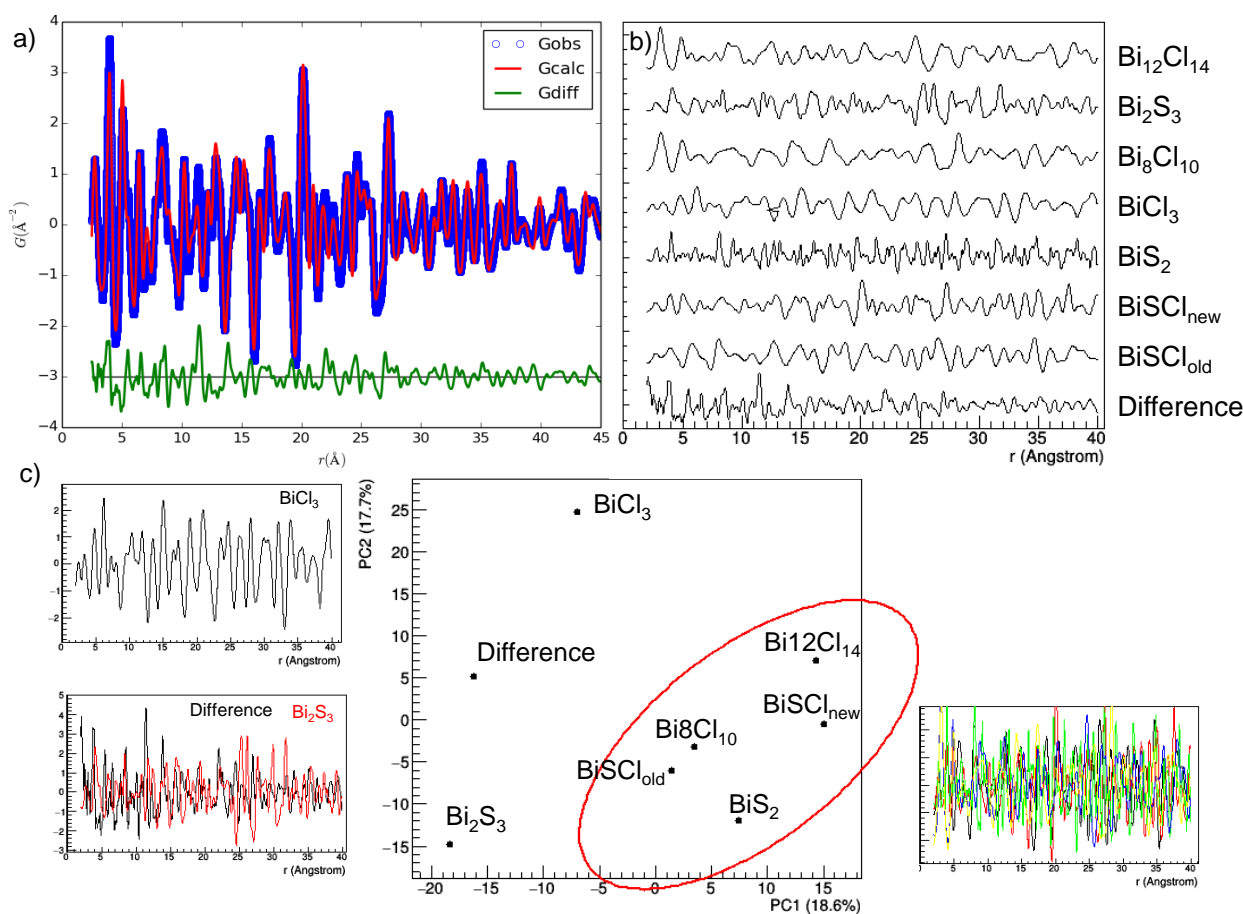
Figure S28. PDF-based analysis to identify impurities in the BiSCl sample. The difference profile resulting from the fit of the measured PDF profile with the crystal phase identified in this study (here referred to as BiSCl$_{new}$; panel a) was compared with the PDF profiles calculated from the crystal phases of likely impurities (panel b). The principal component analysis applied to the data matrix shown in panel b produced the score plot of the first two principal components (PC1 and PC2), where the representative points of the crystal phases were placed according to the similarity of their PDF profiles (panel c), which are grouped in three clusters as a result of a hierarchical clustering procedure based on the Melhanobious distances of the representative points. It results that none of the considered impurities has a PDF profile close to the Difference profile. The ICSD codes of the considered impurities are the following:

ICSD n. 100173 - BiSCl$_{old}$ (the known crystal phase for BiSCl)
ICSD n. 7801 – BiS$_2$
ICSD n. 2866 – BiCl$_3$
ICSD n. 30775 – Bi$_2$S$_3$
ICSD n. 414236 – Bi$_8$S$_{10}$
ICSD n. 9225 – Bi$_{12}$Cl$_4$

Table S5. Comparison of the structural parameters and energy differences between inclusion (SOC) and neglect (noSOC) of Spin Orbit Coupling in BiSCl. The geometrical parameters refer to the newly discovered polymorph of BiSCl. DFT optimized crystal structure of the newly discovered polymorph of BiSCl is shown below.

Property	SOC	noSOC
Energy difference between polymorphs of BiSCl (noSOC geometry)	9.1 meV/atom	10.5 meV/atom
Energy difference between polymorphs of BiSCl (optimized geometry)	8.9 meV/atom	10.5 meV/atom
Distance Bi-Bi	3.981 Å	3.977 Å
Distance Bi-S1	2.757 Å	2.748 Å
Distance Bi-S2	2.637 Å	2.640 Å
Distance Bi-S3	4.892 Å	4.885 Å
Distance Bi-Cl	2.900 Å	2.896 Å
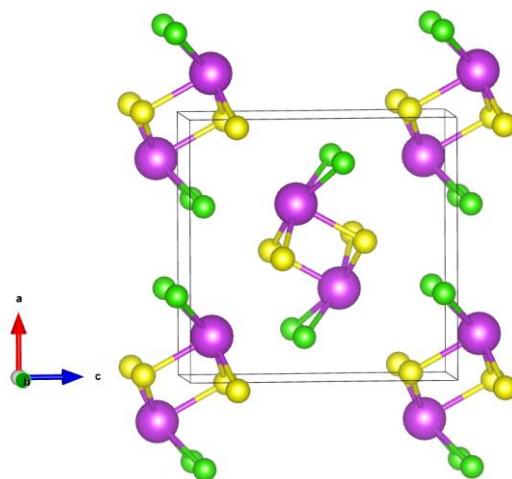
Optical Absorption Properties of the Bi chalcohalide NCs and their Calculated Electronic Structure.
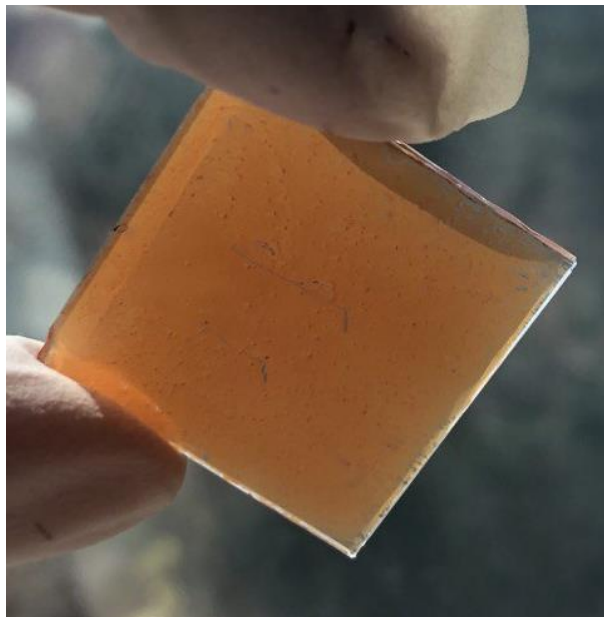
Figure S29. Picture of a BiSBr NC film used to measure transmittance and reflectance.
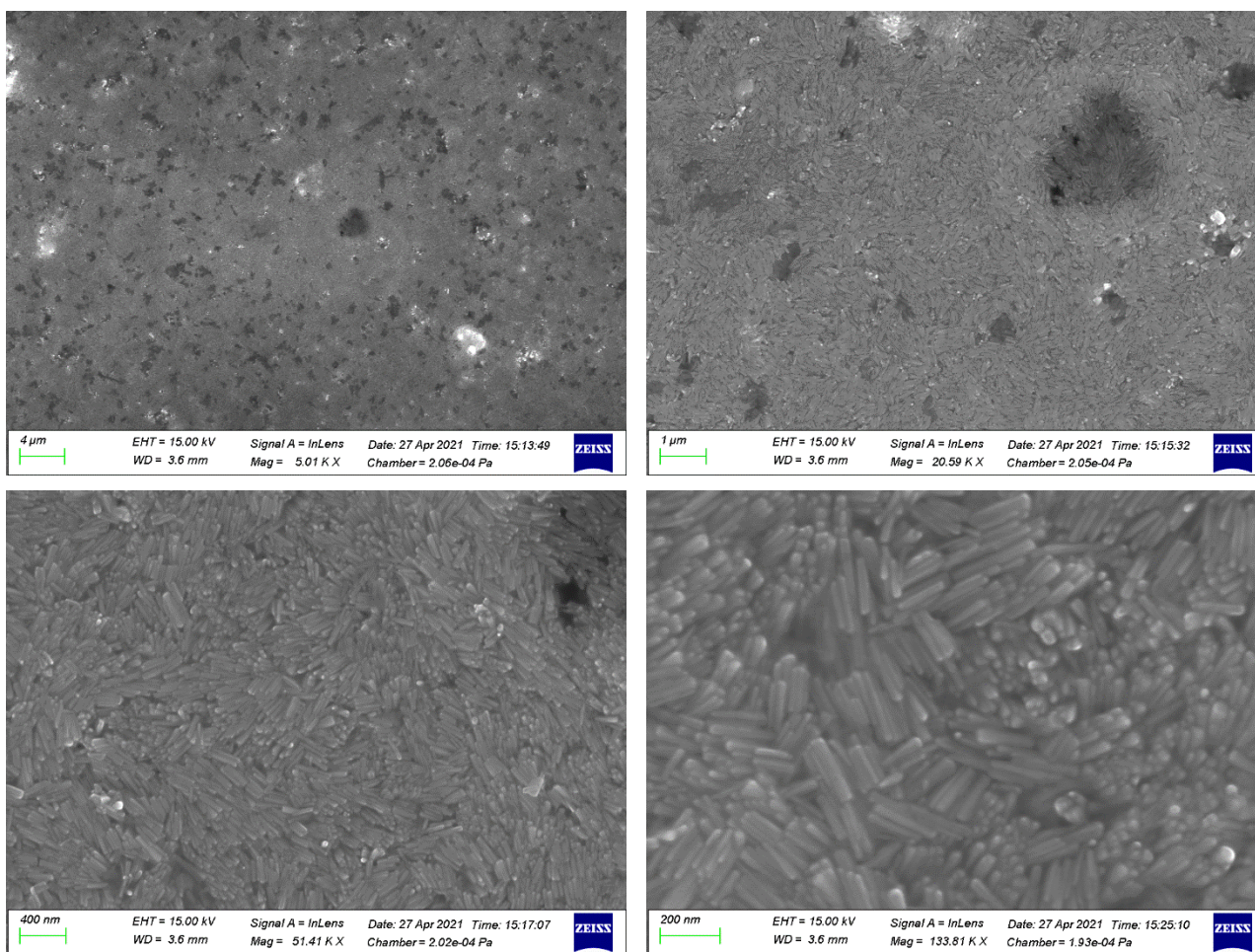
Figure S30. SEM images of a BiSBr NC film.
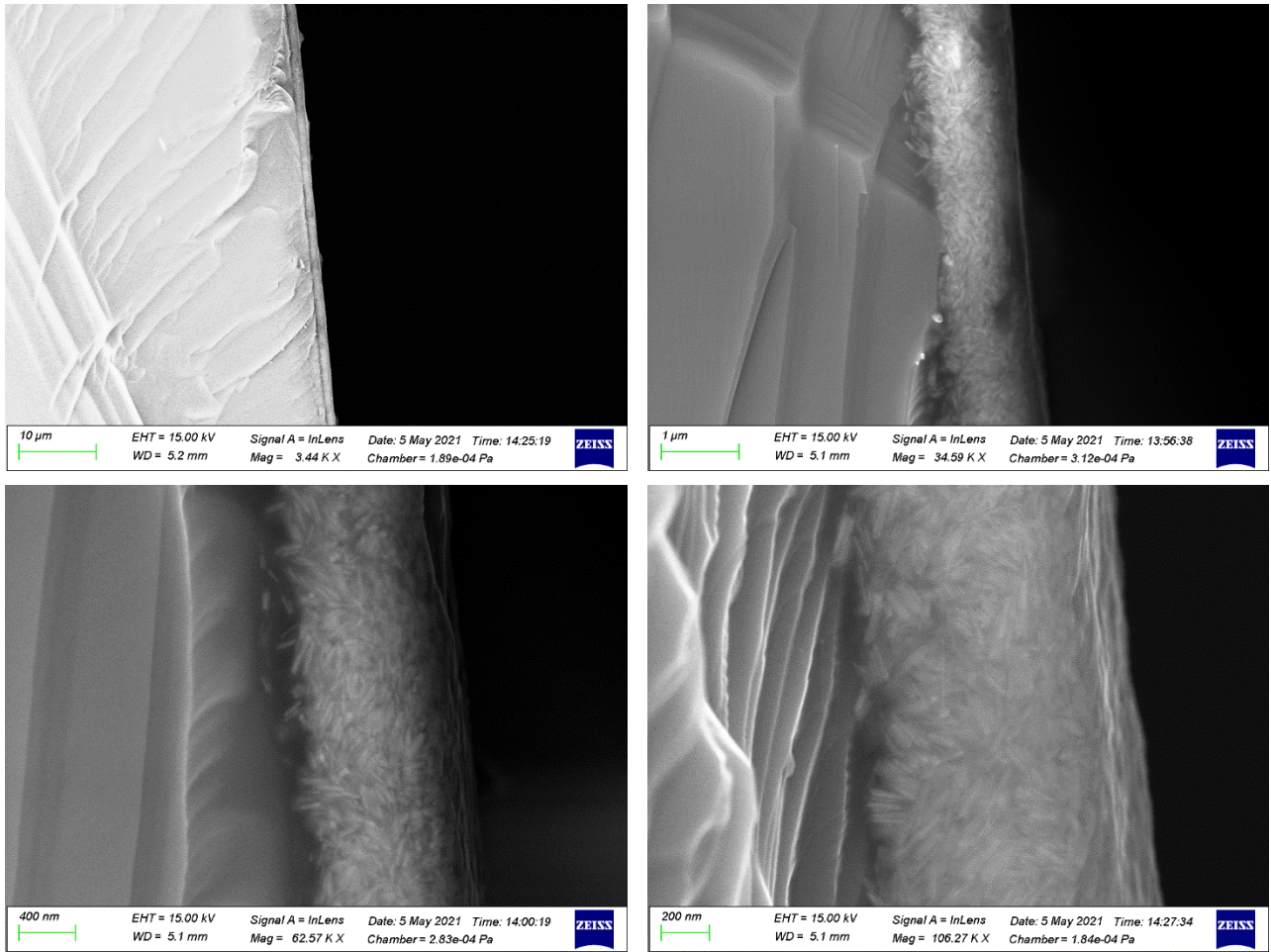
Figure S31. SEM images of the cross section of a BiSBr NC film.
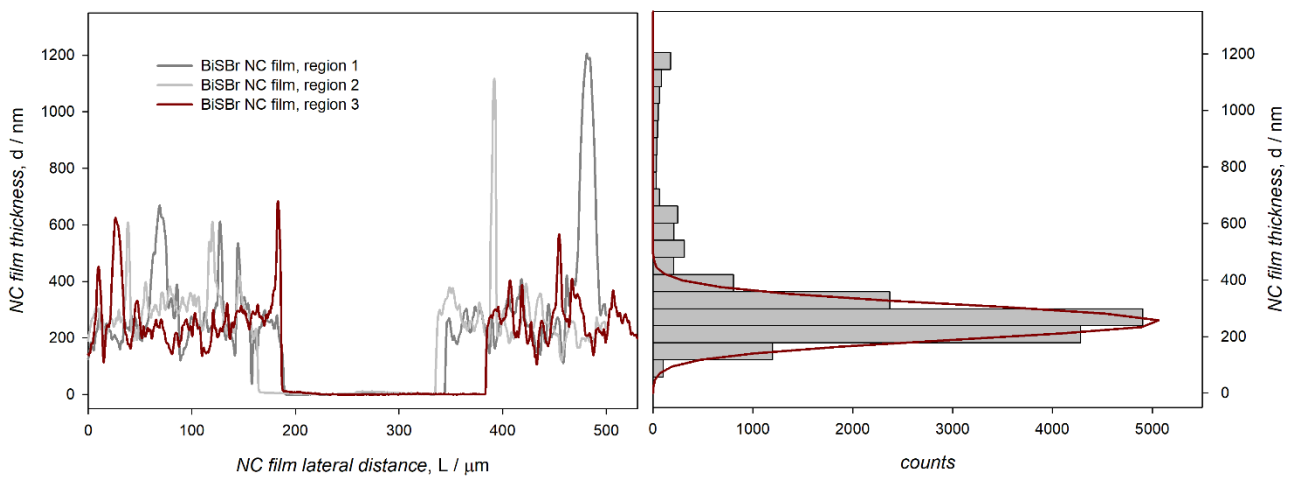
Figure S32. Thickness of the above shown BiSBr NC film in three different regions and thickness distribution.
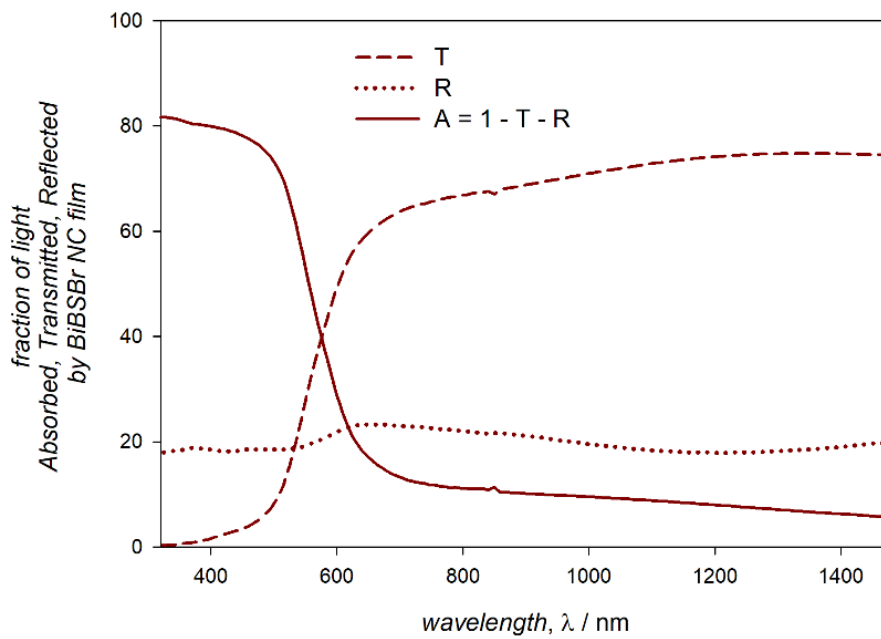
Figure S33. Transmittance, reflectance, and absorptance of the above shown BiSBr NC film.
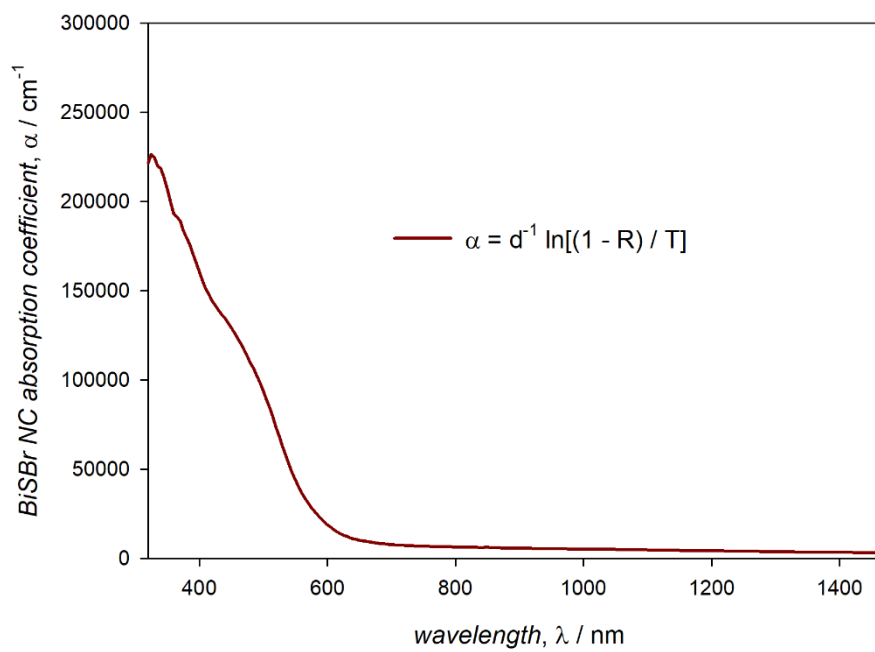
Figure S34. Absorption coefficients of the above shown BiSBr NC film.
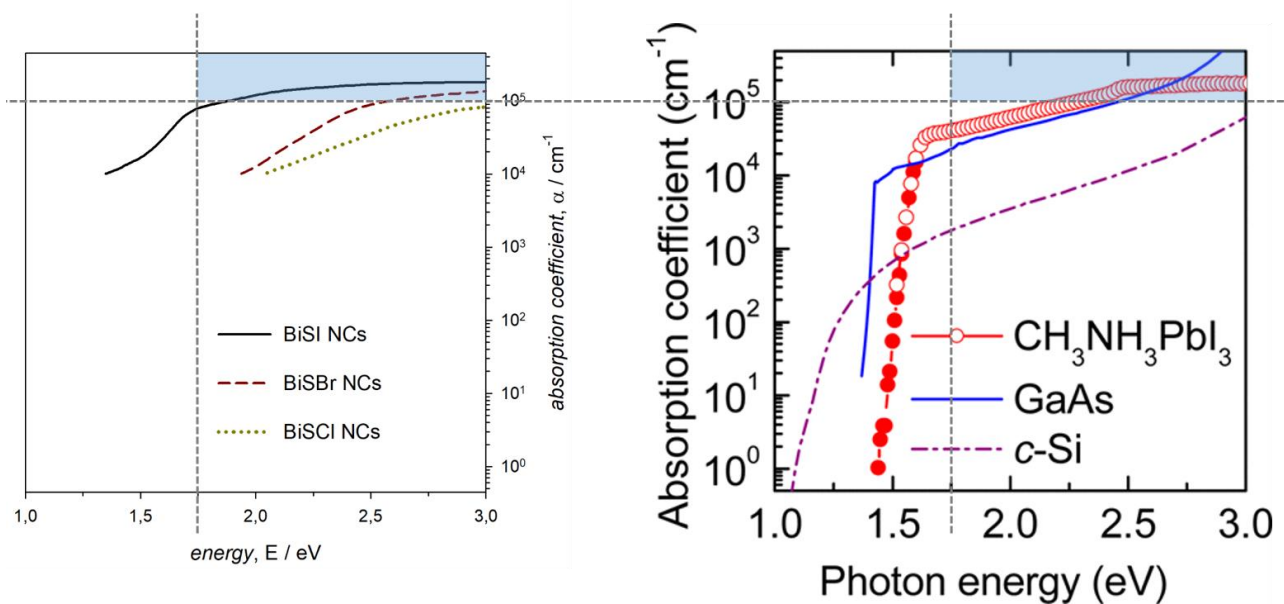
Figure S35. Absorption coefficients of the BiSX NC films compared with those of methylammounium lead iodide perovskite, gallium arsenide, and silicon (copied from ref. S28 with permission from the ACS).
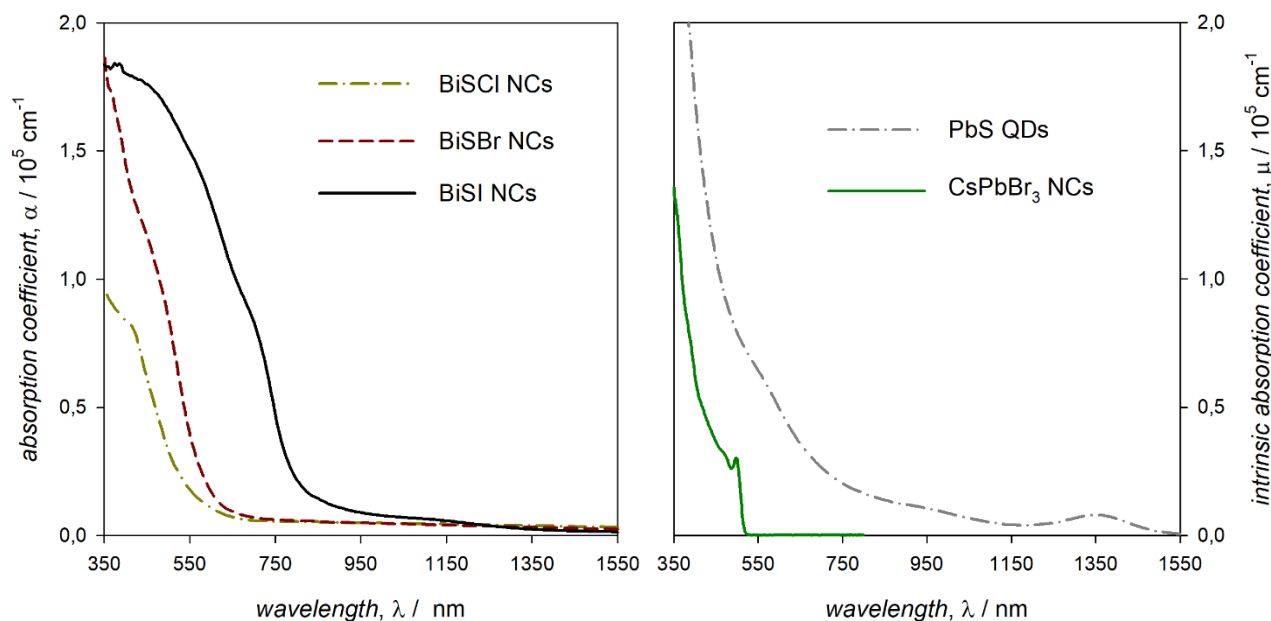
Figure S36. Absorption coefficients, α, of the BiSX NC films compared with the intrinsic absorption coefficients, μ, of dispersions of 4.9 nm diameter PbS QDs and 8.6 nm diameter CsPbBr₃ NCs.[S29,S30]

.
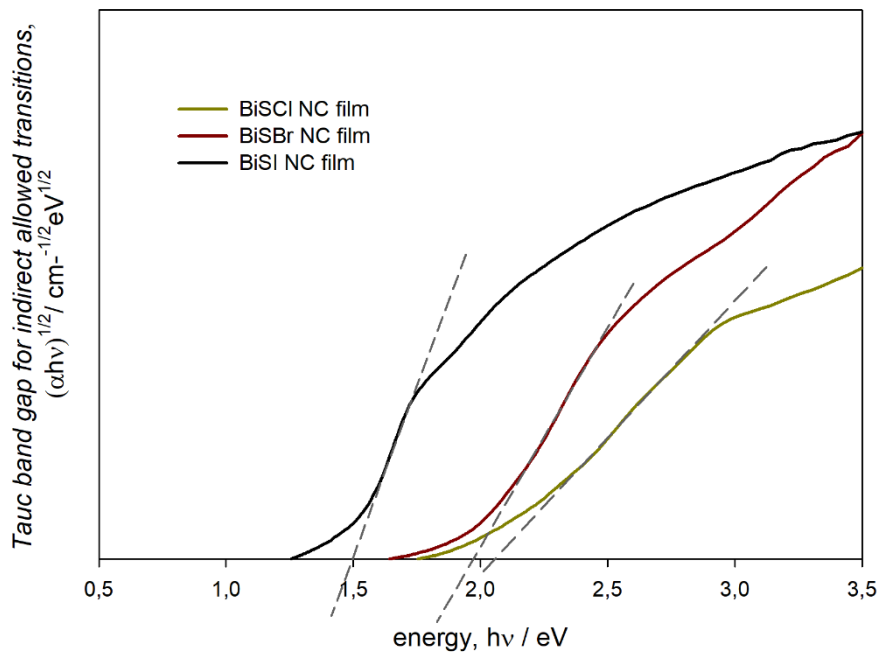
Figure S37. Linear fit of the absorption edge of BiSX NC films according to the Tauc representation for estimating the band gap in the case of indirect, allowed transitions.
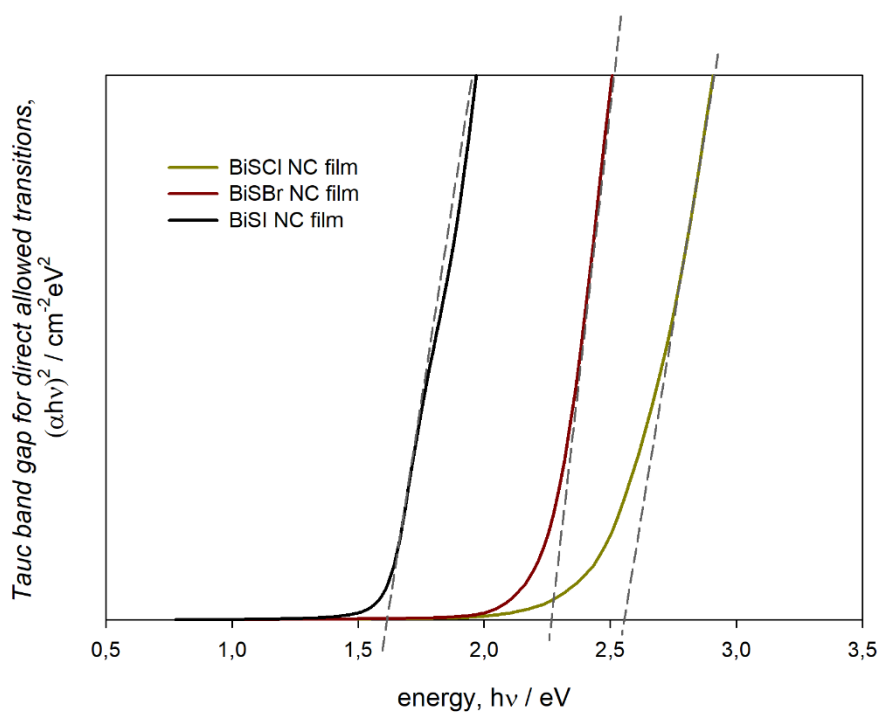
Figure S38. Linear fit of the absorption edge of BiSX NC films according to the Tauc representation for estimating the band gap in the case of direct, allowed transitions.
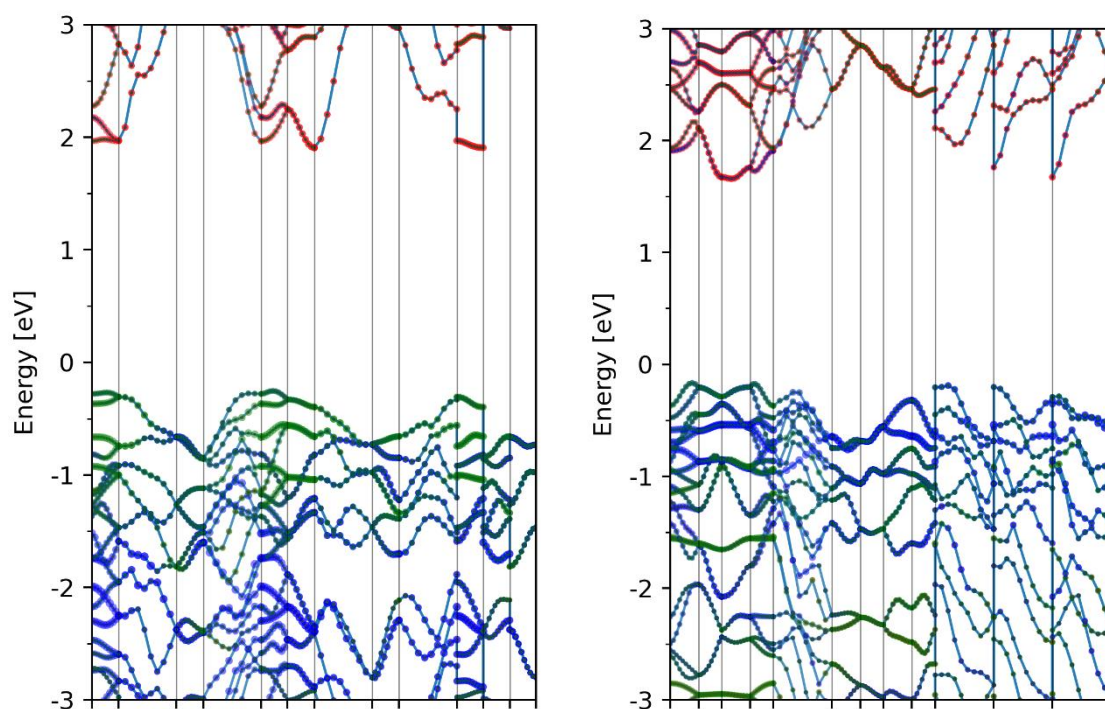
Figure S39. Band structures for BiSCl (left) and BiSI (right). Red, green, and blue represent the projections onto Bi, S, and the halogen atoms.
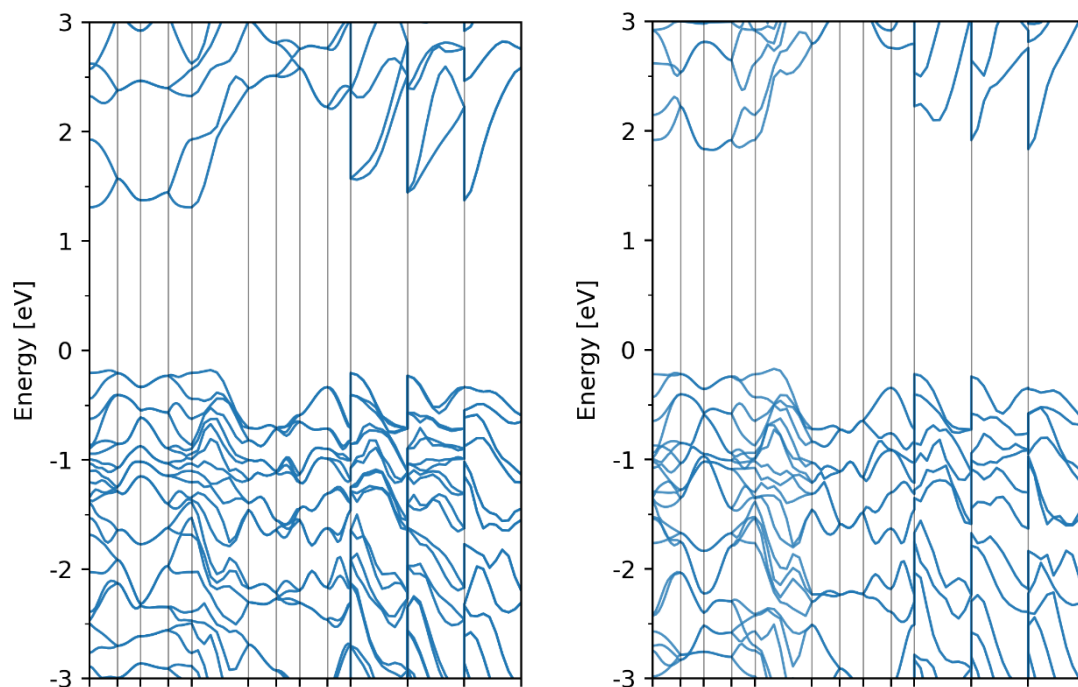
Figure S40. Comparison of the BiSBr band structures calculated with (left) and without (right) the spin-orbit coupling.
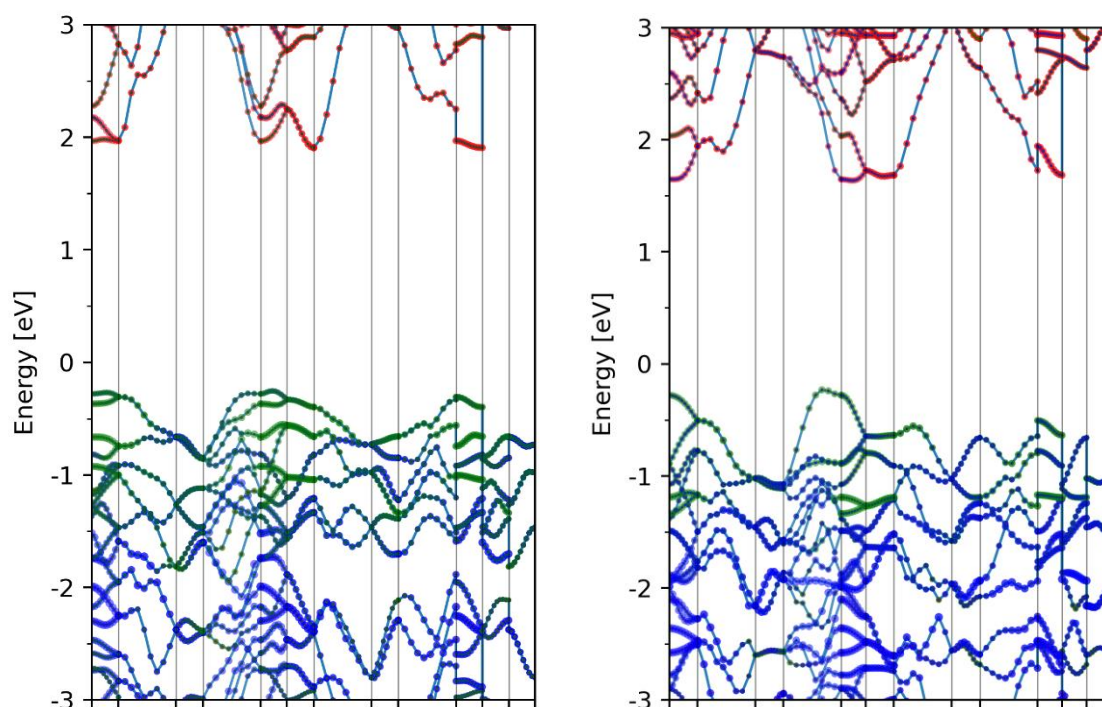
Figure S41. Band structures for our BiSCl polymorph (left) and the known BiCl polymorph (right). Red, green, and blue represent the projections onto Bi, S, and the halogen atoms.
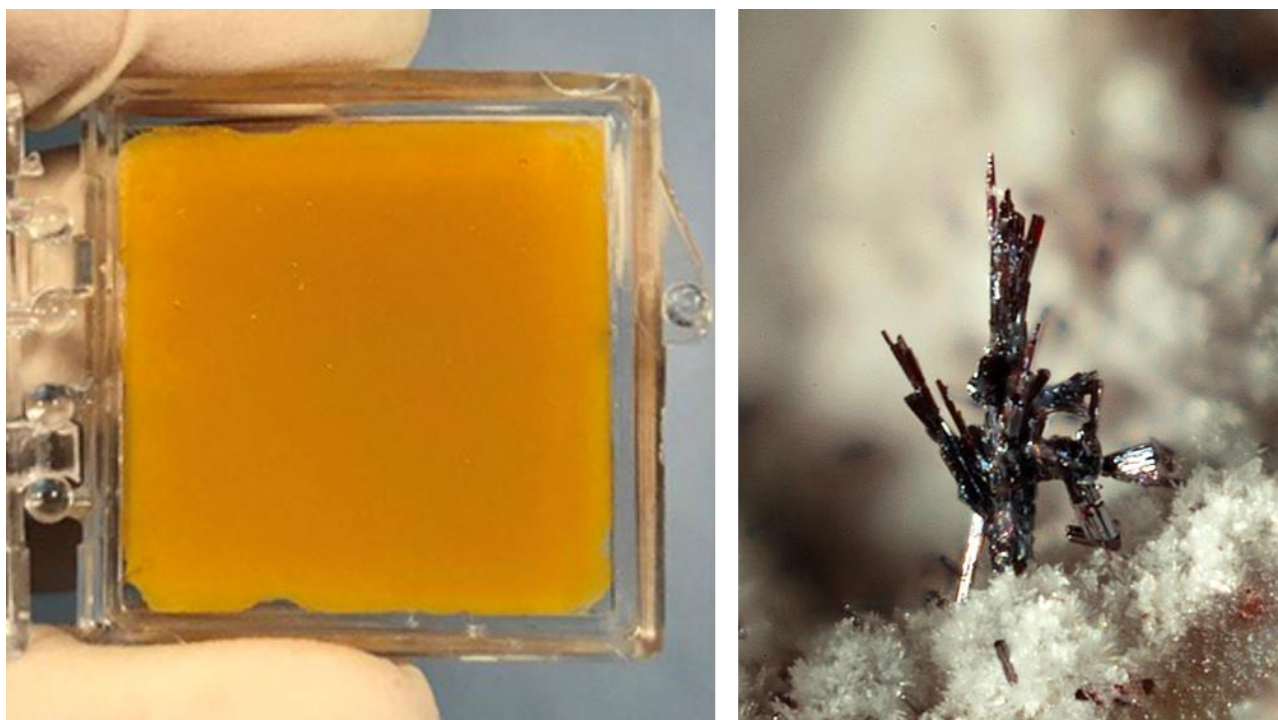

Figure S42. Daylight picture of a film of our BiSCl NCs (left) and of a crystal of the naturally occurring BiCl polymorph (right; Demicheleite-(Cl) BiSCl - La Fossa crater, Vulcano Island, Lipari, Eolie Islands, Messina Province, Sicily, Italy. Group of little prismatic and elongated tabular red-gray metallic crystals of demicheleite-(Cl) up to 0.35 mm (analyzed). Photo Enrico Bonacina (OLYMPUS DIGITAL CAMERA); Collection Domenico Preite; Copyright © Enrico Bonacina – Creative Commons Non-Commercial Share Alike Licence - Some Rights Reserved).

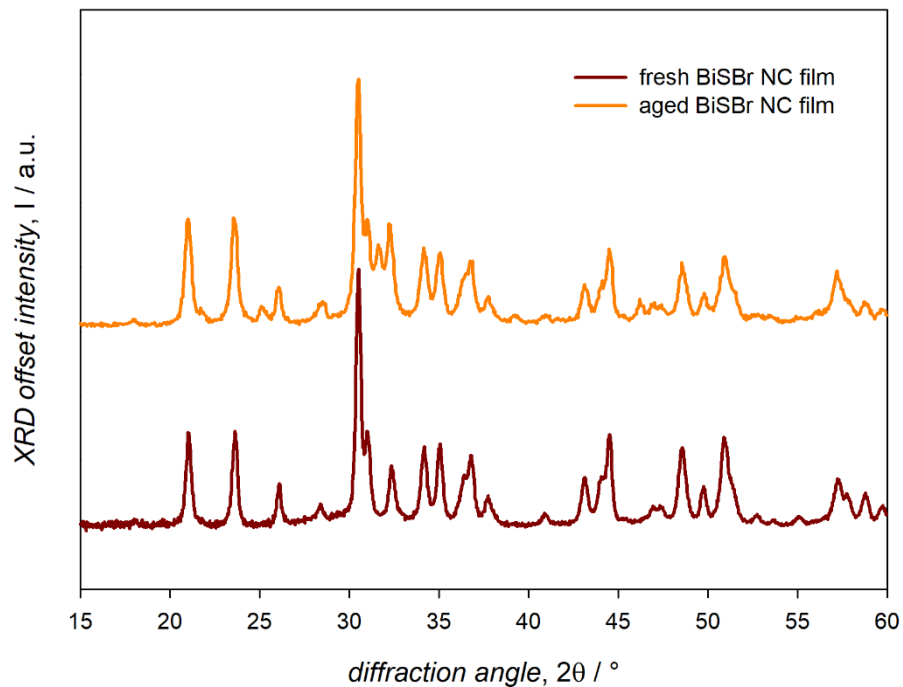**Colloidal and Structural Stability of the Bi chalcohalide NCs.**

Figure S43. XRD patterns upon long term storage at ambient conditions of a BiSBr NC film deposited on a Si substrate.

Figure S44. Daylight pictures of toluene dispersions of BiSBr NCs capped with oleate ligands (left vial), which were exchanged for dimethyldidodecylammonium bromide (middle vial) and dodecanethiol (right vial).
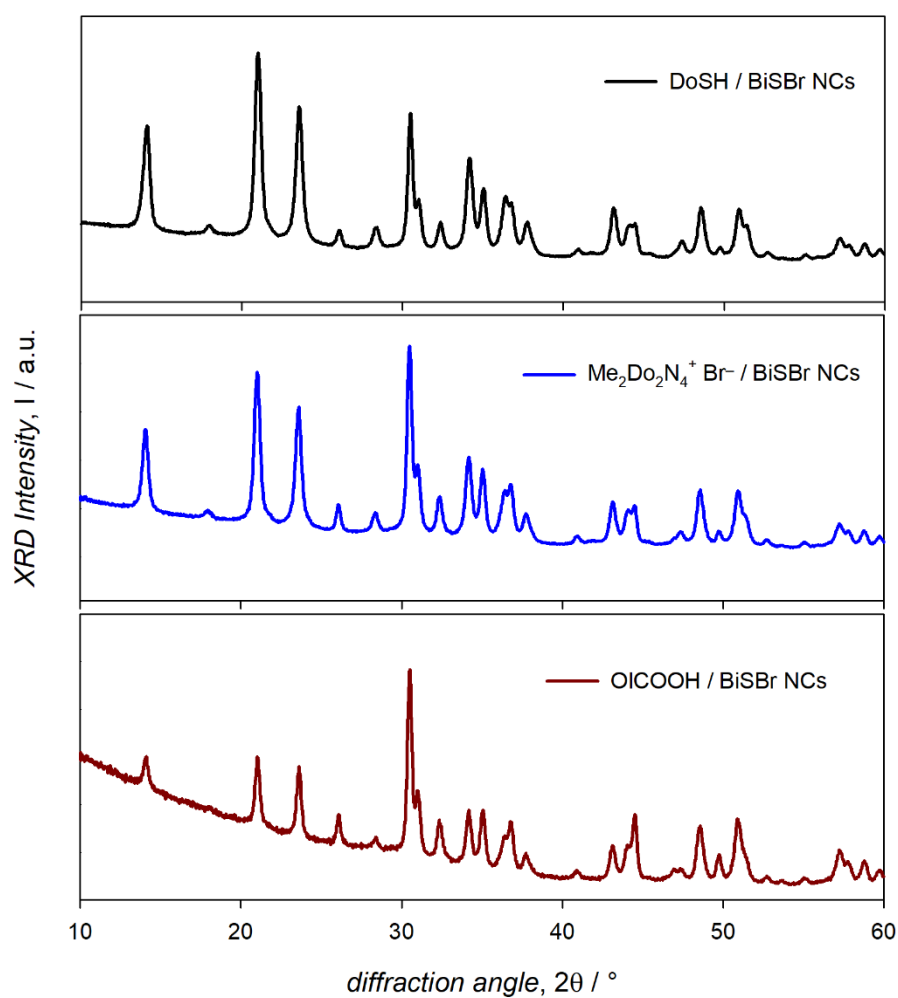

Figure S45. XRD pattern of BiSBr NCs capped with oleate ligands (bottom panel), which were exchanged for dimethyldidodecylammonium bromide (middle panel) and dodecanethiol (top panel).

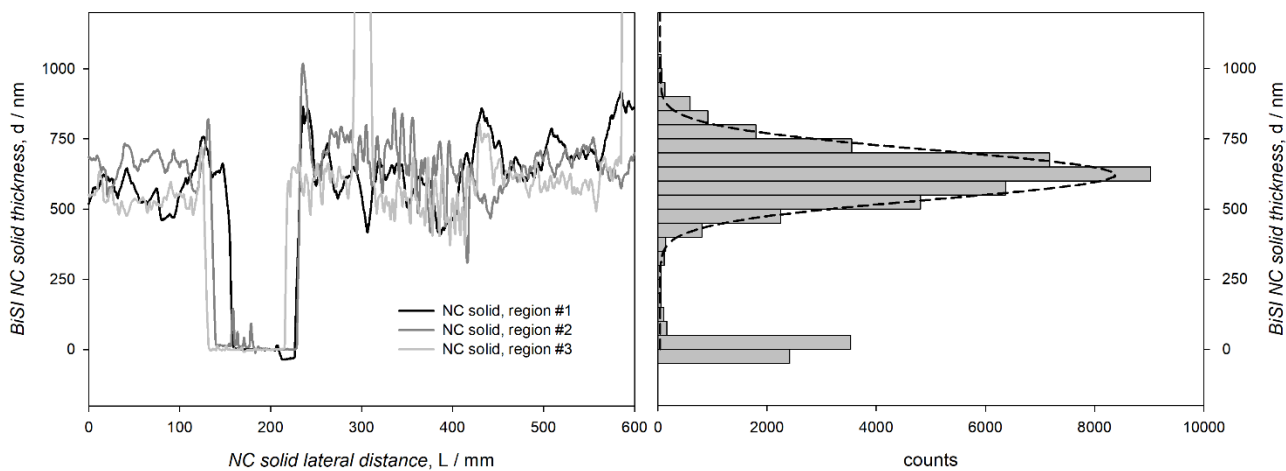**Photoelectrodes based on the Bi chalcohalide NCs.**

Figure S46. Thickness of a BiSI NC photoelectrode in three different regions and thickness distribution.
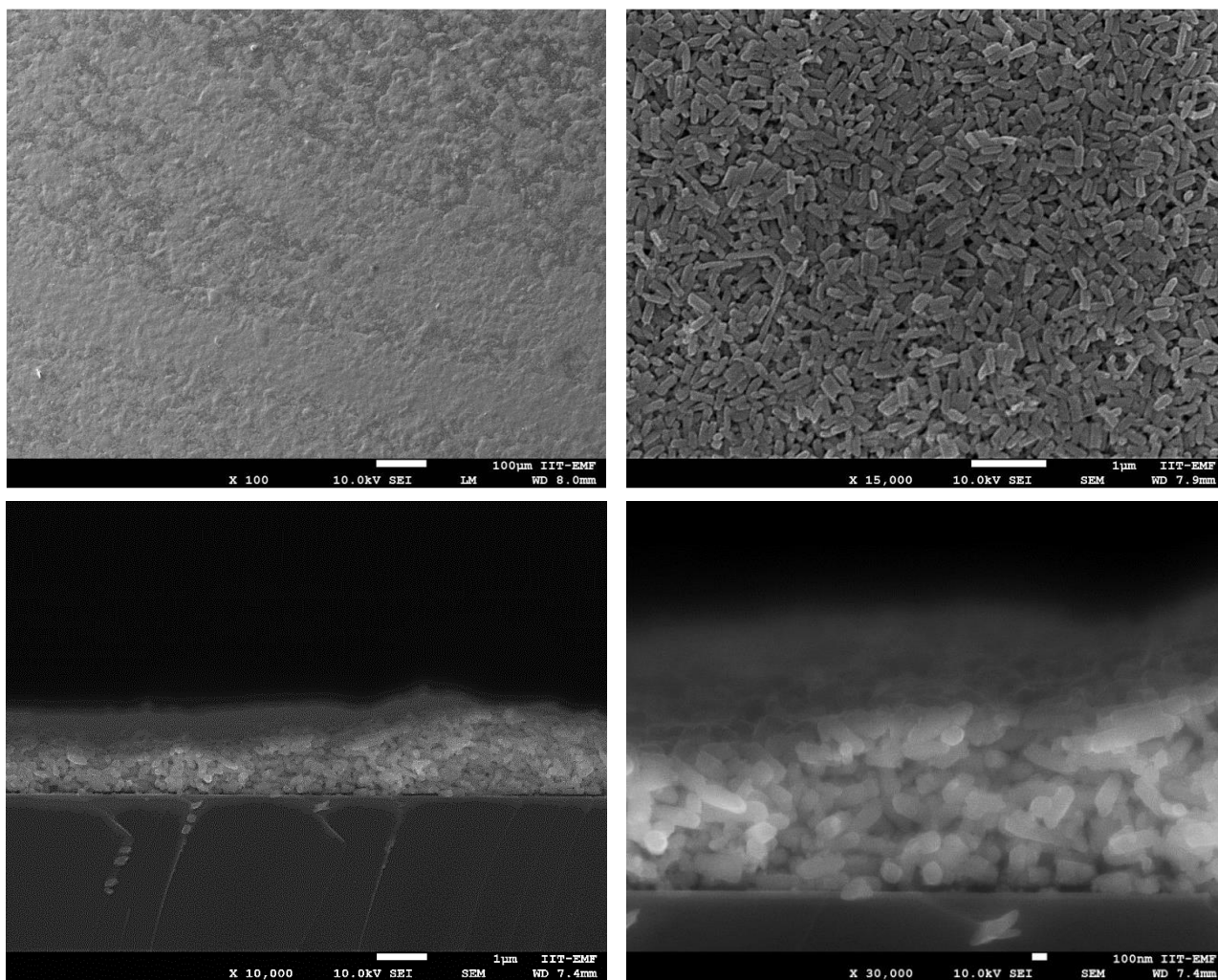

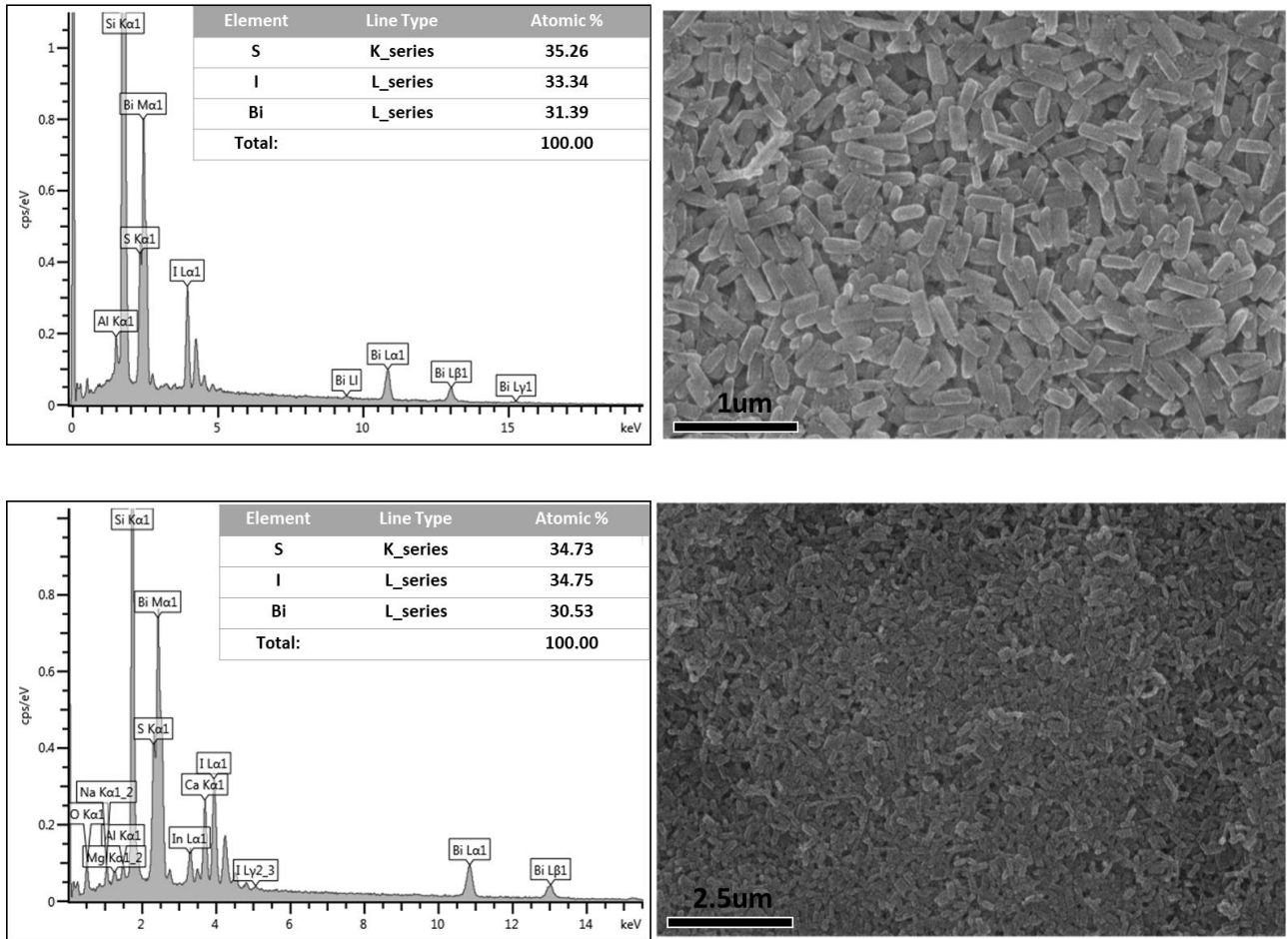**Figure S47.** SEM images of the BiSI NC solid film deposited on ITO.

Figure S48. SEM-EDS data for the BiSI NC solid films: EDS spectra and related elemental composition of the BiSI NC solid films fabricated on Si (top) and on ITO (bottom).
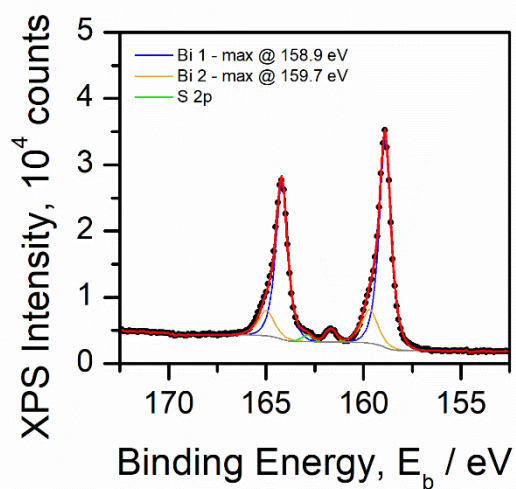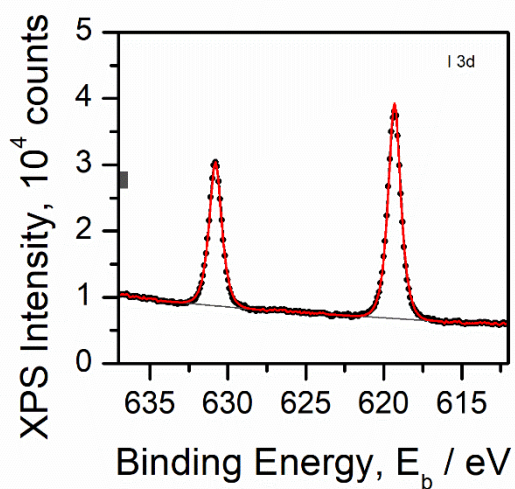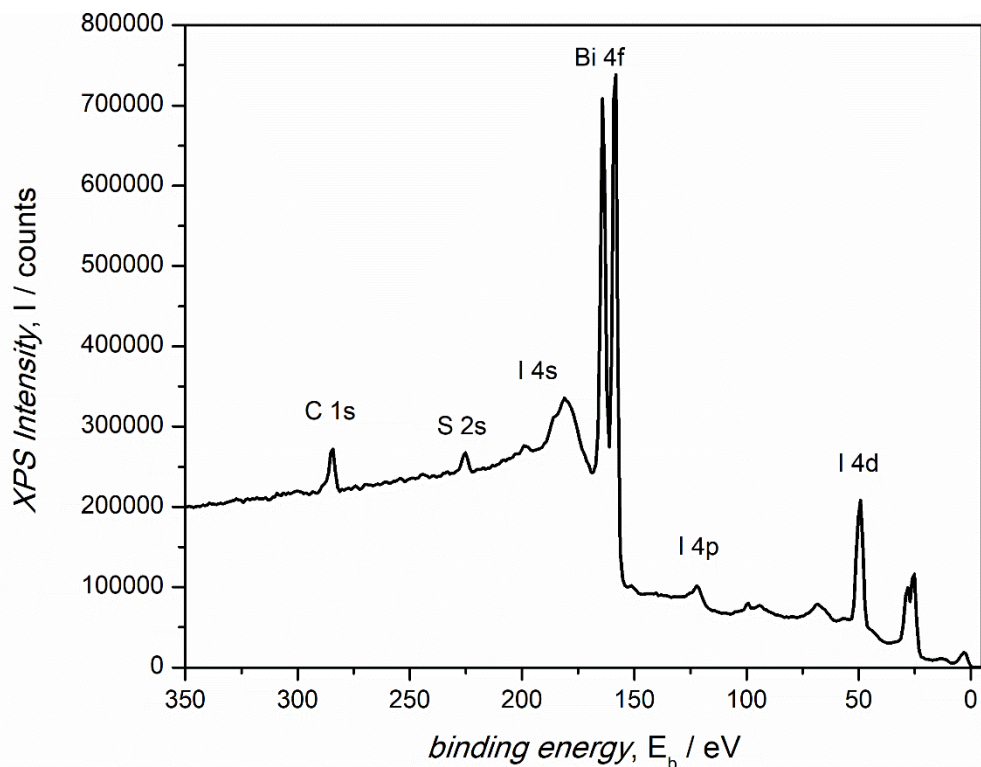
Figure S49. top) XPS spectrum of a BiSI NC solid film on Si. bottom) high-resolution XPS spectra showing details of the I 3d region (left) and of the Bi 4f and S 2p region (right); the Bi 4f region shows the presence of a minor component consistent with Bi(III) species, along with a main component ascribable to BiSI. Such a minor component could be related either to surface Bi atoms that experience different surroundings from the inner Bi atoms and/or to the presence of amorphous species (which could hardly be eliminated by the layer-by-layer approach use to fabricate NC solid films).
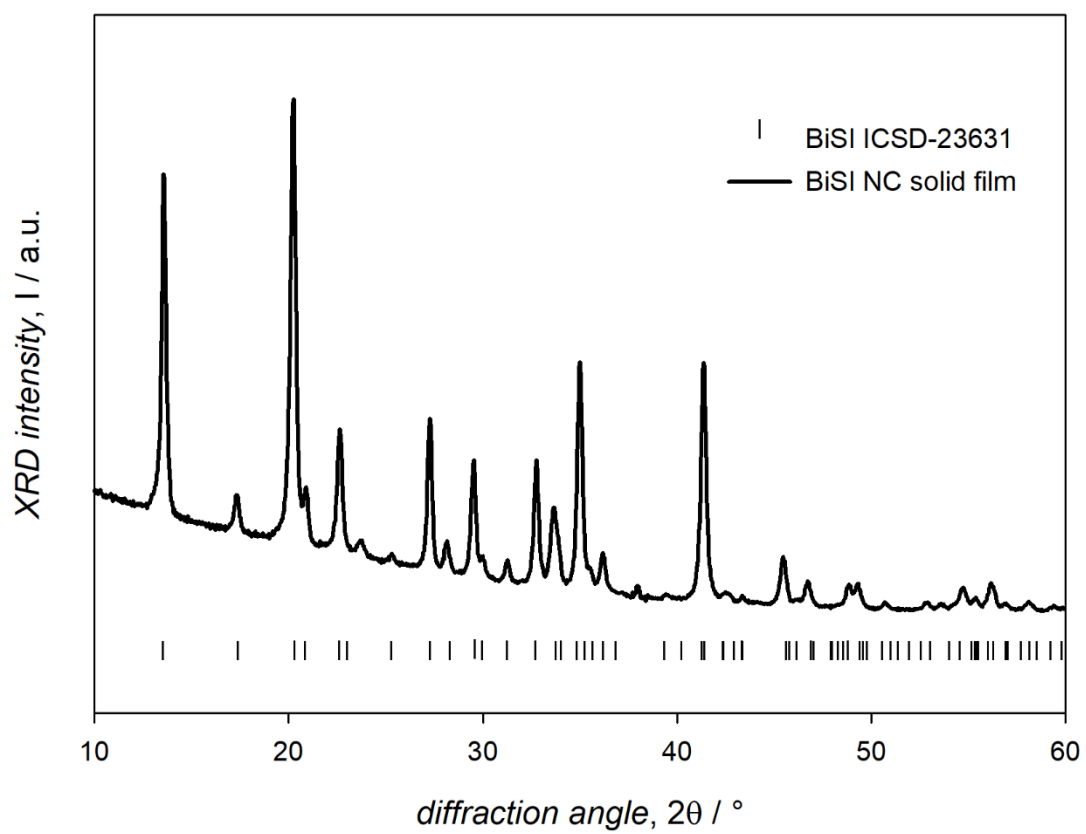
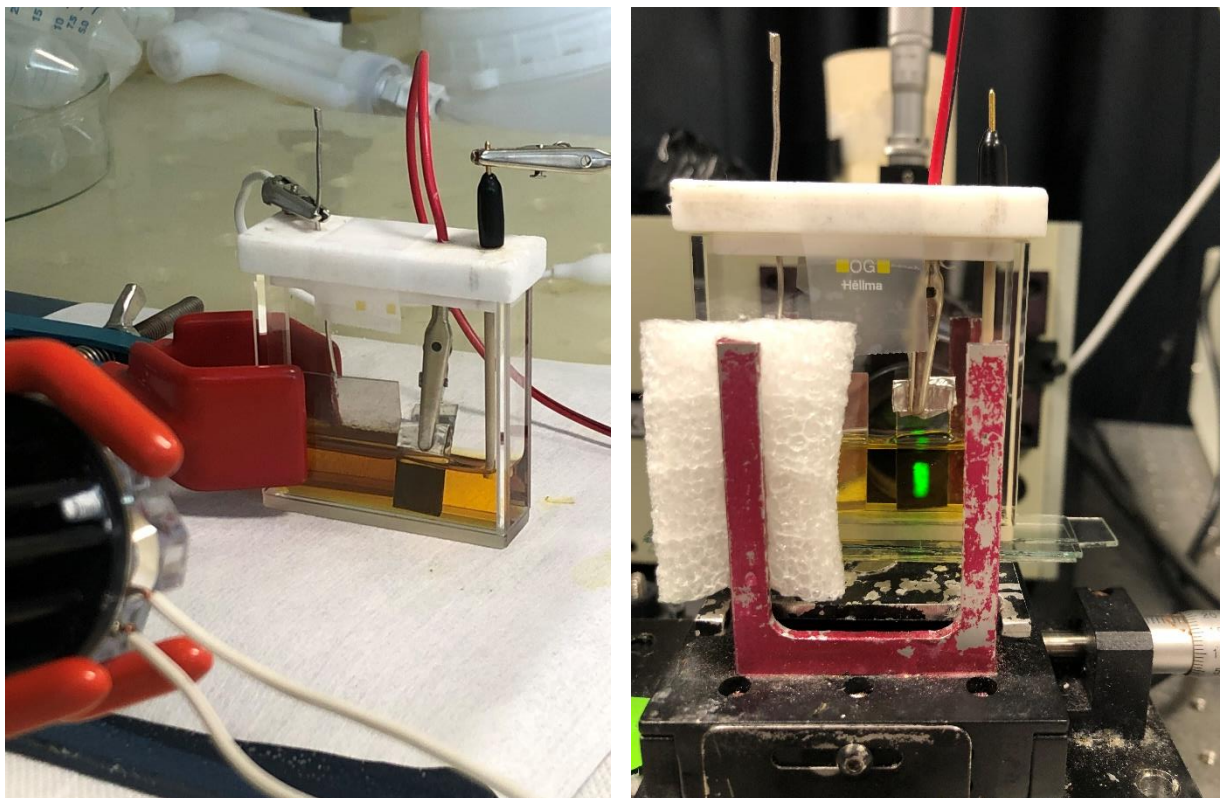**Figure S50.** XRD pattern of a BiSI NC solid film fabricated on Si.

Figure S51. Daylight pictures of the photoelectrochemical setup.
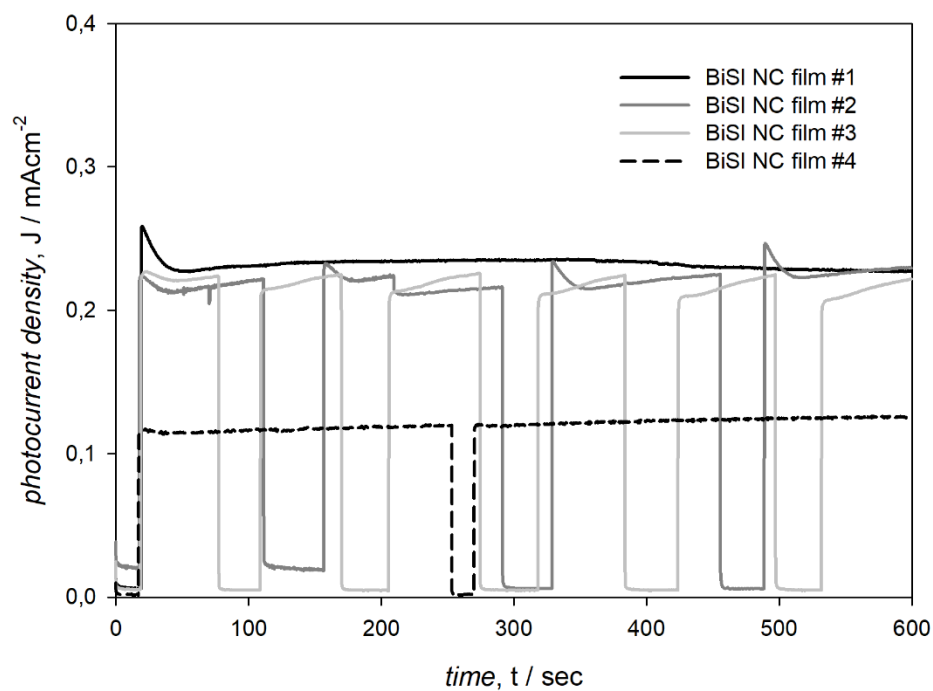
Figure S52. Photocurrent density extracted at a 0.25 V bias under solar-simulated illumination for four different BiSI NC solids other than that shown in Figure 5b.
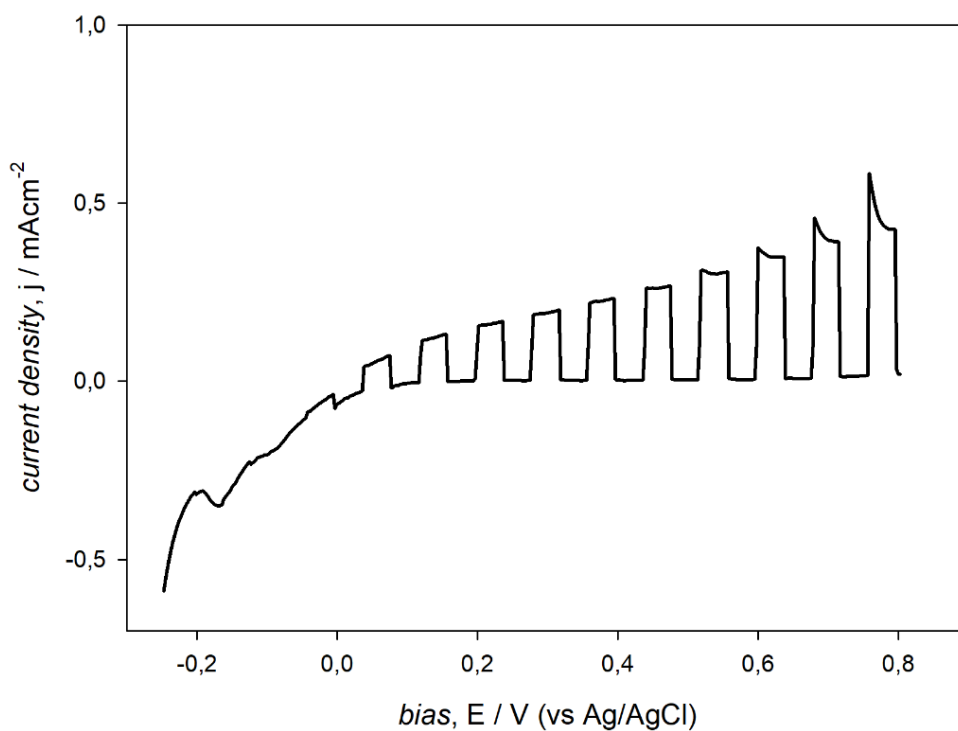
Figure S53. Chopped current density/voltage plot of a BiSI NC solid under solar simulated illumination.

Figure S54. IPCE at a 0.25 V bias under monochromatic illumination for three different BiSI NC solids other than that shown in Figure 5c.

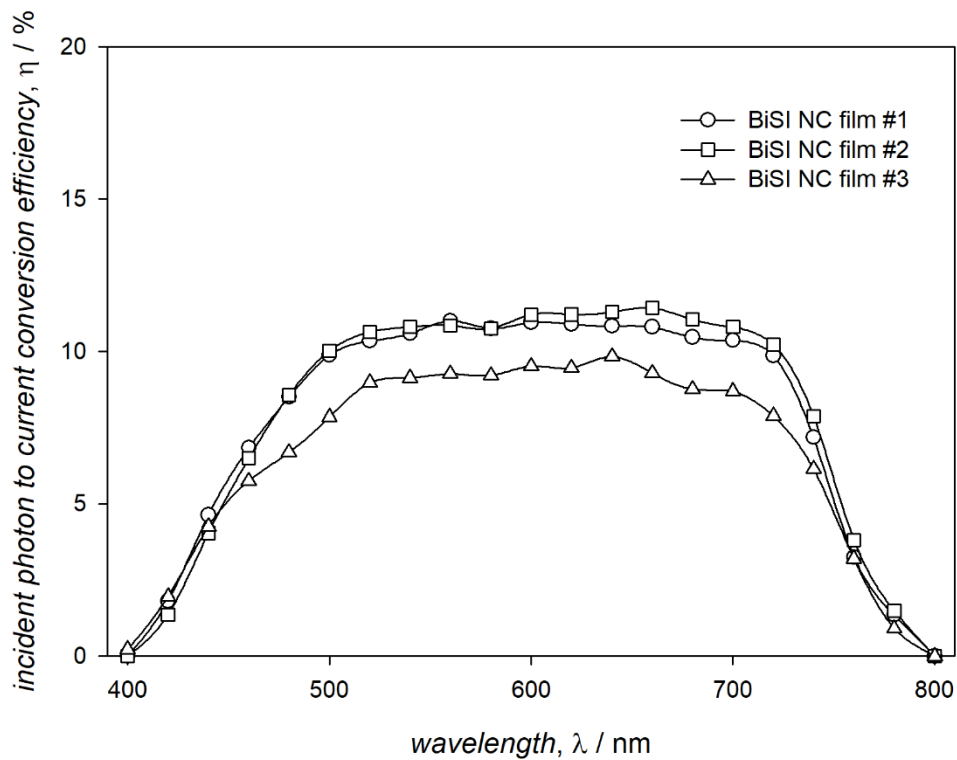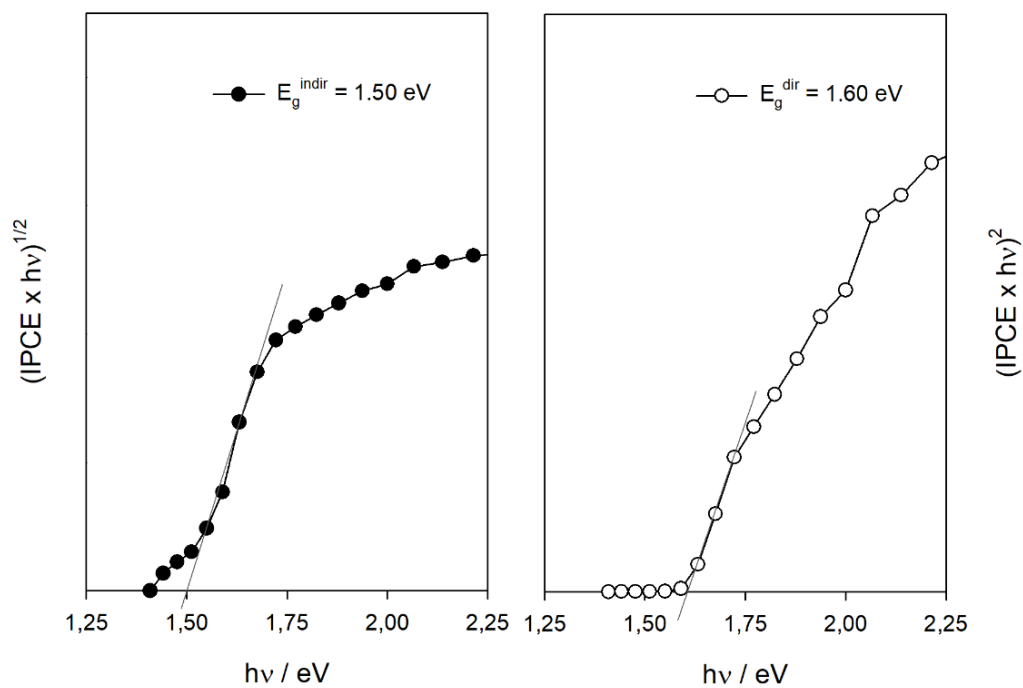**Figure S55.** Estimation of the direct and indirect band gap of the BiSI NC solids by Tauc analysis of the IPCE.
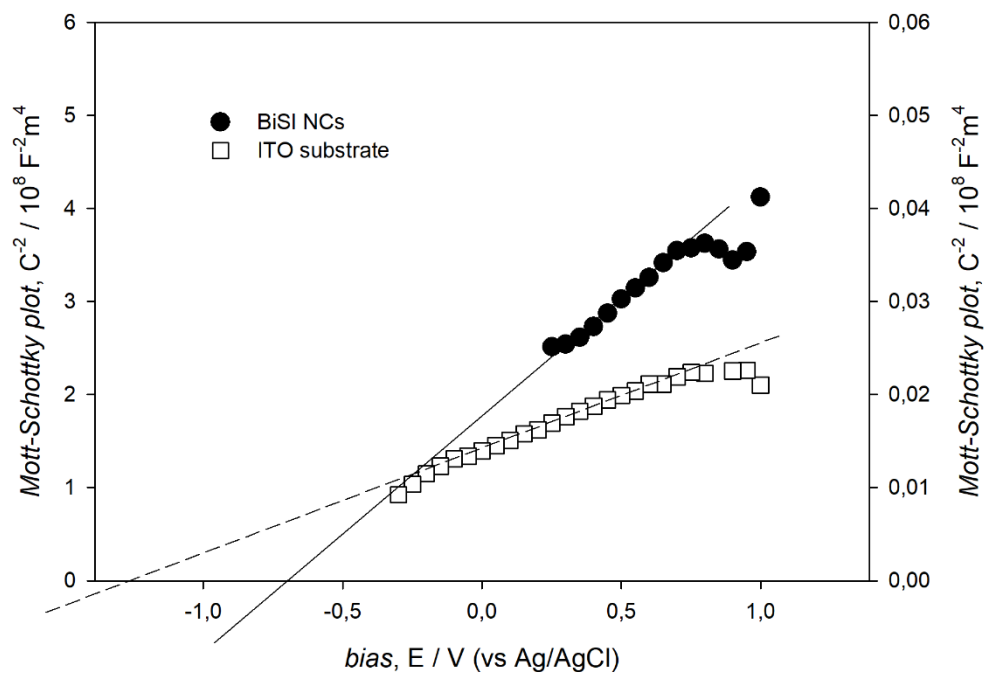
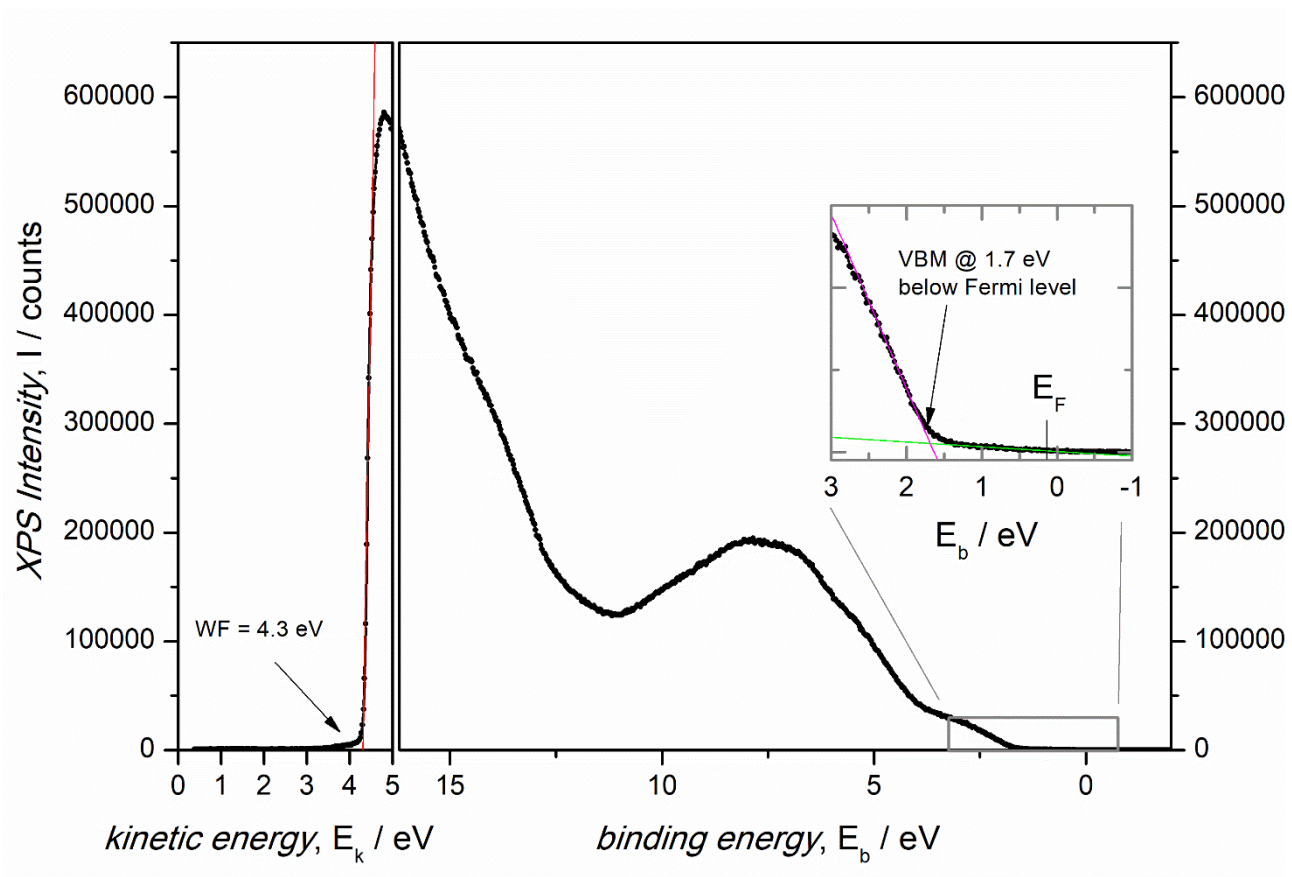**Figure S56.** Mott-Schottky plots of a BiSI NC solid and a bare ITO substrate.

Figure S57. UPS spectrum of a BiSI NC solid.

Supporting References.

S1.   M. Imran, V. Caligiuri, M. Wang, L. Goldoni, M. Prato, R. Krahne, L. De Trizio, L. Manna, Benzoyl Halides as Alternative Precursors for the Colloidal Synthesis of Lead-Based Halide Perovskite Nanocrystals, *J. Am. Chem. Soc.* **2018**, *140*, 2656–2664.

S2.   A. P. Hammersley, S. O. Svensson, M. Hanfland, D. Hauserman, Two-dimensional detector software: From real detector to idealised image or two-theta scan. *High Press. Res.* **1996**, *14*, 235–248.

S3.   P. Juhás, T. Davis, C. L. Farrow, S. J. L. Billinge, PDFgetX3: a rapid and highly automatable program for processing powder diffraction data into total scattering pair distribution functions. *J. Appl. Cryst.* **2013**, *46*, 560–566.

S4.   A. Altomare, N. Corriero, C. Cuocci, A. Falcicchio, A. Moliterni, R. Rizzi, QUALX2.0: a qualitative phase analysis software using the freely available database POW_COD. *J. Appl. Cryst.* **2015**, *48*, 598-603.

S5.   S. Gražulis, A. Daškevič, A. Merkys, D. Chateigner, L. Lutterotti, M. Quirós, N. R. Serebryanaya, P. Moeck, R. T. Downs, A. Le Bail, Crystallography Open Database (COD): an open-access collection of crystal structures and platform for world-wide collaboration. *Nucleid Acids Research* **2012**, *40*, D420-427.

S6.   J. Faber, T. Fawcett, The powder diffraction file: present and future. *Acta Cryst. B* **2002**, *58*, 325.

S7.   S. N. Kabekkodu, J. Faber, T. Fawcett, New Powder Diffraction File (PDF-4) in relational database format: advantages and data-mining capabilities. *Acta Cryst. B*, **2002**, *58*, 333.

S8.   T. Degen, M. Sadki, E. Bron, U. König, G. Nénert, The HighScore suite. *Powder Diffraction* **2014**, *29(S2)*, S13.

S9.   A. Altomare, C. Cuocci, C. Giacovazzo, A. Moliterni, R. Rizzi, N. Corriero, A, Falcicchio, EXPO2013: A Kit of Tools for Phasing Crystal Structures from Powder Data. *J. Appl. Cryst.* **2013**, *46*, 1231.

S10. C. L. Farrow, P. Juhás, J. W. Liu, D. Bryndin, E. S. Božin, J. Bloch, T. Proffen S. J. L. Billinge, PDFfit2 and PDFgui: computer programs for studying nanostructure in crystals. *J. Phys.: Condens. Matter* **2007**, *19*, 335219.

S11. J .Rodríguez-Carvajal, Recent advances in magnetic structure determination by neutron powder diffraction. *Phys. B: Condensed Matter* **1993**, *192*, 55.

S12. P. Juhás, C. L. Farrow, X. Yang, K. R. Knox S. J. L. Billinge Complex modeling: a strategy and software program for combining multiple information sources to solve ill posed structure and nanostructure inverse problems. *Acta Cryst. A* **2015**, *71*, 562.

S13. H .M. Rietveld, A profile refinement method for nuclear and magnetic structures. *J. Appl. Cryst.* **1969**, 2, 65.

S14. L. B. McCusker, R. B. Von Dreele, D. E. Cox, D. Louer, P. Scardi, Rietveld refinement guidelines. J. *Appl. Cryst.* **1999**, *32*, 36.

S15. R .Caliandro, D. B. Belviso, RootProf: software for multivariate analysis of unidimensional profiles. *J. Appl. Cryst.* **2014**, *47*, 1087.

S16. J. Tauc, R. Grigorovici, A. Vancu, Optical Properties And Electronic Structure of Amorphous Germanium. *Phys. Status Solidi B* **1966**, *15*, 627.

S17. E .Davis, N. Mott, Conduction in non-crystalline systems V. Conductivity, optical absorption and photoconductivity in amorphous semiconductors. *Philos. Mag.* **1970**, *22*, 0903.

S18. Q. A. Akkerman, M. Gandini, F. Di Stasio, P. Rastogi, F. Palazon, G. Bertoni, J. M. Ball, M. Prato, A. Petrozza, L. Manna, Strongly emissive perovskite nanocrystal inks for high-voltage solar cells. *Nat. Energy*, **2017**, *2*, 16194.

S19. G. Kresse, J. Furthmüller, Efficiency of ab-initio total energy calculations for metals and semiconductors using a plane-wave basis set. *Comput. Mater. Sci.* **1996**, *6*, 15.

S20. P. E. Blöchl, Projector augmented-wave method. *Phys. Rev. B* **1994**, *50*, 17953.

S21. J. P. Perdew, K. Burke, M. Ernzerhof, Generalized Gradient Approximation Made Simple. *Phys. Rev. Lett.* **1996**; *77*, 3865.

S22. A. Tkatchenko, M. Scheffler, Accurate Molecular Van Der Waals Interactions from Ground-State Electron Density and Free-Atom Reference Data. *Phys. Rev. Lett.* **2009**, *102*, 073005.

S23. K. Momma, F. Izumi, VESTA 3 for three-dimensional visualization of crystal, volumetric and morphology data. *J. Appl. Cryst.* **2011**, *44*, 1272.

S24. A. Altomare, G. Campi, C. Cuocci, L. Eriksson, C. Giacovazzo, A. Moliterni, R. Rizzi, P. Werner, Advances in Powder Diffraction Pattern Indexing: N-TREOR09. *J. Appl. Cryst.* **2009**, *42*, 768–775.

S25. P. M. de Wolff, A simplified criterion for the reliability of a powder pattern indexing. *J. Appl. Cryst.* **1968**, *1*, 108–113.

S26. A. Altomare, R. Caliandro, M. Camalli, C. Cuocci, I. Da Silva, C. Giacovazzo, A. Moliterni, R. Spagna, Space-group determination from powder diffraction data: A probabilistic approach. *J. Appl. Cryst.* **2004**, *37*, 957–966; A. Altomare, M. Camalli, C. Cuocci, I. Da Silva, C. Giacovazzo, A. Moliterni, R. Rizzi, Space group determination: Improvements in EXPO2004. *J. Appl. Cryst.* **2005**, *38*, 760–767; A. Altomare, M. Camalli, C. Cuocci, C. Giacovazzo, A. Moliterni, R. Rizzi, Advances in space-group determination from powder diffraction data. *J. Appl. Cryst.* **2007**, *40*, 743–748.

S27. A. Altomare, C. Cuocci, C. Giacovazzo, A. Moliterni, R. Rizzi, Powder diffraction: The new automatic least-squares Fourier recycling procedure in EXPO2005. *J. Appl. Cryst.* **2006**, *39*, 558–562.

S28. S. De Wolf, J. Holovsky, S.-J. Moon, P. Löper, B. Niesen, M. Ledinsky, F.-J. Haug, J.H. Yum, C. Ballif Organometallic Halide Perovskites: Sharp Optical Absorption Edge and Its Relation to Photovoltaic Performance *J. Phys. Chem. Lett.* **2014**, *5*, 1035–1039.

S29. D. Debellis, G. Gigli, S. ten Brinck, I. Infante, C. Giansante Quantum-Confined and Enhanced Optical Absorption of Colloidal PbS Quantum Dots at Wavelengths with Expected Bulk Behavior *Nano Lett.* **2017**, *17*, 1248–1254.

S30. D. Quarta, M. Imran, A.-L. Capodilupo, U. Petralanda, B. van Beek, F. De Angelis, L. Manna, I. Infante, L. De Trizio, C. Giansante Stable Ligand Coordination at the Surface of Colloidal CsPbBr3 Nanocrystals *J. Phys. Chem. Lett.* **2019**, *10*, 3715–3726.